Damping in CMOS-MEMS Resonators

by

Jay Brotz

Master's Project Report

in

Electrical & Computer Engineering

at

Carnegie Mellon University

Advisor: Professor Gary Fedder

Second Reader: Dr. Tamal Mukherjee

June, 2004

Abstract

This research examines the energy loss in micromechanical resonators fabricated in a CMOS-MEMS process. Characterization and understanding of energy loss is a first step to optimal design in MEMS mixer and filter applications. The known energy loss mechanisms for micromechanical resonators - air damping, acoustic anchor loss, thermoelastic damping, and internal friction - are discussed. Theory is given to support expected levels of damping for air damping and thermoelastic damping; design methods to reduce energy loss are discussed for acoustic anchor loss. Squeeze-film and Stoke's damping in electrostatic gap resonators are analyzed over varying pressure. A tuning fork method and a quarter-wavelength method for reducing acoustic anchor loss are given. Cantilever and fixed-fixed resonator topologies are designed in order to test for air damping and acoustic anchor loss. Air damping theory matches the measured data from 10 μTorr to atmospheric pressure with 25%-69% error. The quality factor becomes fixed in value for pressures below about 500 mTorr. The cantilever tuning fork shows a decrease in damping by 67% over a single cantilever and the fixed-fixed tuning fork by 73% over a single fixed-fixed beam. The free-free beam provided a minimal decrease in damping. Thermoelastic damping is theoretically shown to be negligible for beam widths smaller than 5 μm, and internal friction is believed to be negligible as well, although it has not been quantifiable to this point.

Abstract 3
1 Introduction 5
2 Theory of Energy Loss 10
2.1Air damping 12
2.2Acoustic anchor loss 20
2.3Thermoelastic damping 24
2.4Internal losses 28
3 Resonator Design 30
3.1Chip Design 30
3.2Basic Topologies 35
3.2.1Cantilever 35
3.2.2Fixed-fixed beam 39
3.3Design for Resonant Frequency 41
3.4Design for Better Quality Factor 42
3.4.1Minimization of anchor loss 42
3.5Design for Gain and Fabrication Issues 47
4 Testing and Results 52
4.1On-Chip Amplifier Design 52
4.2Testbed 55
4.3Measured Transfer Functions 59
4.4Data Analysis 63
4.4.1Pressure Dependence of Quality Factor 63
4.4.2Anchor Design Dependence of Quality Factor 65
5 Conclusions 69
Appendix A: Calculation of Resonant Frequency 72

A.1 Static Method 72

A.2 Dynamic Method 76

References 78

Figure 1.1 CMOS-MEMS process **8**
Figure 2.1 Squeeze-film dimensions **15**
Figure 2.2 Simulated air damping quality factor for the TSMC cantilever; dotted line: contribution from squeeze-film damping, dashed line: contribution from Stoke's damping, solid line: total air damping quality factor **18**
Figure 2.3 Equivalent circuit for bending vibration, (a.) cantilever beam, (b.) two-port model, (c.) mechanical impedance model **22**
Figure 2.4 Thermoelastic quality factor as a function of frequency (w=1µm); solid line: silicon dioxide, dashed line: aluminum **27**
Figure 2.5 Thermoelastic quality factor as a function of beam width (f=1 MHz); solid line: silicon dioxide, dashed line: aluminum **28**
Figure 3.1 TSMC test chip "actuators77a" (a.) layout (b.) optical microscope image **31**
Figure 3.2 Jazz test chip "jz60_002" (a.) layout (b.) optical microscope image **32**
Figure 3.3 TSMC cantilever (a.) diagram (b.) scanning-electron micrograph **37**
Figure 3.4 Jazz cantilever (a.) diagram (b.) scanning-electron micrograph **38**
Figure 3.5 Jazz fixed-fixed beam (a.) diagram (b.) scanning-electron micrograph **40**
Figure 3.6 Jazz cantilever tuning fork (a.) diagram (b.) scanning-electron micrograph **43**
Figure 3.7 Jazz fixed-fixed tuning fork **43**
Figure 3.8 Resonant frequency of cantilever tuning fork with respect to width of the cross-beam **45**
Figure 3.9 Jazz free-free beam (a.) diagram (b.) scanning-electron micrograph **47**
Figure 3.10 Effect of mask misalignment on CMOS-MEMS beam: (a.) designed straight-sidewall beam; (b.) mask misalignment of (a.); (c.) designed stepped-sidewall beam; (d.) misalignment of (c.) **50**
Figure 3.11 Fixed-fixed beam with snap-in electrode **50**

Figure 3.12 Microsurgery gap clearing (a.) Before FIB (b.) After FIB **51**
Figure 4.1 Fully differential on-chip amplifier **53**
Figure 4.2 Differential test system **54**
Figure 4.3 Diagram of test system **56**
Figure 4.4 Photograph of MEMS PCB **57**
Figure 4.5 External amplifier PCB (a.) schematic (b.) photograph **58**
Figure 4.6 Testing system (a.) vacuum chamber (b.) test equipment **59**
Figure 4.7 Raw data for fixed-fixed tuning fork: Real and Imag -- with DC bias; F Real and F Imag -- with DC bias = 0 on output gap (feedthrough) **60**
Figure 4.8 Resonant peaks of each resonator @ 100 mTorr 64
Figure 4.9 Quality factor of the TSMC and Jazz cantilevers as a function of air pressure **66**
Figure A.1 Diagrams of a.) cantilever and b.) fixed-fixed beams **75**

Acknowledgements

I thank Dr. Fang Chen for his help with processing and operating the FIB, Suresh Santhanum for the training for and use of his vacuum chamber, Dr. John Neumann for his assistance in many areas but notably in wirebonding, and Michael Sperling with advice on circuit design. I thank Mary Moore for assistance in innumerable ways and for running the lab in an impeccable manner. I thank Lynn Philibin and Elaine Lawrence for help with graduate affairs.

1 Introduction

Current RF receiver systems, such as in cellular phones, use large, off-chip capacitors, inductors, and crystal or SAW oscillators to filter incoming signals. These components limit the miniaturization of portable devices and increase the cost of manufacturing due to parts assembly and packaging. Complimentary metal-oxide-silicon microelectromechanical systems (CMOS-MEMS) have the opportunity to create the next generation in miniaturized, inexpensive integrated RF filters. A CMOS-MEMS bandpass filter, based on micromechanical resonators that are on the same substrate as the receiver circuitry, is much smaller and more easily integrable, allowing cheaper, smaller portable wireless devices.

Micromechanical resonators can be used as a filtering element in electronics because of their vibrational transfer function. When a vibrating beam is underdamped, it will displace much more at its natural frequency than at any other frequency, giving rise to a resonant peak. The resonant peak in the transfer function of a microresonator leads to its use as a filter or a mixer-filter [1-2] in-line with electronics for electrostatic actuation and capacitive sensing. To be a part of an effective filter in an electronic

system, microresonators must display certain features such as high out-of-band rejection and steep rolloff, which depend on cyclic energy loss. A useful metric of this energy loss is quality factor, which is the stored energy of a resonator divided by the energy loss per cycle. A high quality factor will not only reduce the attenuation but also improve the shape of the filter's transfer function. This thesis explores quality factor for microresonators made in the CMOS-MEMS process.

A bandpass filter of variable width is created by cascading multiple resonators with "soft" coupling springs. These can be mechanical [3] or electrostatic springs [4]. The rolloff of the bandpass filter increases with the number of cascaded resonators, and the stopband rejection increases with resonator quality factor. Thus, studying the quality factor of microresonators helps in understanding how to design good bandpass filters and identifying the limits of performance for a given process technology.

The known sources of energy loss in micromechanical beam resonators are air damping, acoustic loss through the anchor, thermoelastic damping, and internal friction. Each loss mechanism is independent of the others and may contain several terms due to distinct underlying physical mechanisms. This study compares and contrasts a core set of resonator designs fabricated in the CMOS-MEMS process to devices previously discussed in the literature.

Any communications system that combines MEMS with electronics must connect the two. A single chip containing both is the least expensive and smallest solution. Not

only is the need to wirebond two chips avoided, parasitics are reduced and the ability to array mechanical components with circuitry is created. The CMOS-MEMS process developed at Carnegie Mellon's MEMS Laboratory is an approach that combines circuit integration with simple microstructural fabrication steps [5]. The mechanical components and circuitry are designed within the CMOS layers. The MEMS components are made from the metal interconnect layers and the oxide dielectric layers. The top interconnect metal layer is used as an etch stop to protect the circuitry as well as a top ground plane, which shields the circuitry from radiative interference. After the chips are received from the foundry, release of the moving parts results in the cross-section shown in Figure 1.1. The dielectric is left exposed in places where a gap is intended. A vertical oxide etch removes the overglass and exposed dielectric, exposing the silicon to be etched. A deep reactive ion etch (DRIE) followed by an isotropic silicon etch is then performed to undercut structures surrounded by exposed silicon.

This process has some drawbacks. CMOS processes use stacks of aluminum and silicon dioxide, and so will have greater internal losses than polysilicon or single-crystal silicon. CMOS design rules prevent designing widths and gaps below about 0.5 μm. Full custom processes for RF MEMS passive devices have achieved 100 nm gaps [6]. Yet CMOS-MEMS also has serious advantages in the ability to easily integrate MEMS with circuitry and route interconnects within the mechanical structures. For

FIGURE 1.1 *CMOS-MEMS process*

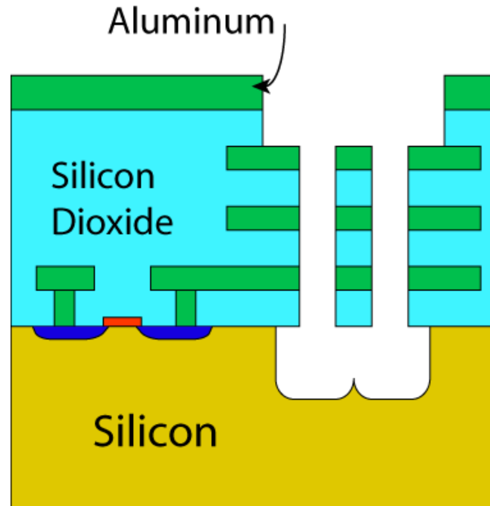

filtering applications, the advantages may outweigh the drawbacks, and so it is being explored for that application.

Electromechanical filters have existed in some capacity since the 1940s [7]. These filters were constructed of metal plates or cylinders several centimeters in size and were coupled with wires. Variations of this have been used up to the present for filtering in the acoustic range and for telephone system single-channel filtering [8]. When analog integrated circuits became sophisticated enough, low-frequency filtering shifted to chips due to size advantage, reliability, and power consumption. Mechanical filters were still used for higher frequency applications and when a very narrow bandwidth and excellent aging properties were necessary. One of the first attempts to fabricate a

thin-film mechanical resonator resulted in the resonant gate transistor pioneered by Westinghouse Research and Development Center in 1967 [9]. Due to poor performance, the resonant gate transistor was not developed further, but in the 1980s, with significant advances in thin-film materials and micromachining techniques, microresonator research began its modern era [10-14].

This thesis is organized by first presenting the theory of energy loss mechanisms and resonator design in Chapter 2. Chapter 3 provides details about the experimental testbed and measured results. The comparisons between theory and results are discussed and other conclusions are made in Chapter 4.

2 Theory of Energy Loss

Each of the known energy loss mechanisms - air damping, acoustic anchor loss, thermoelastic damping, and internal friction - are discussed in this chapter. Analysis of the energy loss mechanisms facilitates design decisions for high-Q resonators. Analytical expressions for the quality factor due to squeeze-film damping, Stoke's damping, and thermoelastic damping are given. Methods to reduce acoustic anchor loss are discussed, and internal friction is discussed. The next chapter describes the design of resonators created to test these energy loss sources.

Quality factor is an expression of the cyclic energy loss in an oscillating system. In terms of energy, it is expressed as the total energy stored the system divided by the energy loss per cycle,

$$Q = \frac{U_{total}}{\Delta U_{loss}}. \tag{2.1}$$

The investigation of resonator quality factor begins with the analysis of a mass-spring-damper system. In the simplest form, the force balance equation is

$$m\ddot{x} + b\dot{x} + kx = F \tag{2.2}$$

where m is mass, b is damping coefficient, k is stiffness, x is displacement, and F is an applied external force. When analyzing free resonance, F is set equal to zero. By normalizing the equation by m, (2.2) can also be written as

$$\ddot{x} + 2\zeta\omega_0\dot{x} + \omega_0^2 x = \frac{F}{m} \tag{2.3}$$

where

$$\zeta = \frac{b}{2m\omega_0} \tag{2.4}$$

and

$$\omega_0 = \sqrt{\frac{k}{m}}. \tag{2.5}$$

ζ is the damping factor and ω_0 is the resonant frequency. The m used in (2.2) through (2.5) is a lumped paramter, and in order to use these equations with a continuous beam, effective mass, m_{eff}, must be used (see Appendix A). When ζ is less than one, the system is underdamped and the damping factor is approximately related to the quality factor by

$$Q = \frac{1}{2\zeta} \tag{2.6}$$

An underdamped system will have a resonant peak in its transfer function that increases in amplitude with greater quality factor and smaller damping factor. The quality factor is measured experimentally by the approximation

$$Q \approx \frac{f_c}{BW_{3dB}}, \tag{2.7}$$

where f_c is the center frequency of the peak, usually referred to as the damped resonant frequency, and BW_{3dB} is the half-power, or 3dB, bandwidth of the measured peak.

This analysis assumes the damping coefficient, b, being proportional to velocity. This is not necessarily the case with all damping mechanisms, as b can be a nonlinear function of velocity in the large-displacement case. The analysis of damping mechanisms in this thesis will assume small displacement.

Energy loss in resonators occurs in the form of many distinct mechanisms. The known sources of dynamic damping in CMOS-MEMS resonators are air damping, acoustic damping through the anchor, internal friction, thermoelastic damping, and coupling between vibrational modes. The first four will be discussed in this thesis. Since energy loss sources add directly for total energy loss, individual quality factors add reciprocally for total quality factor, i.e.,

$$\frac{1}{Q_{tot}} = \frac{1}{Q_1} + \frac{1}{Q_2} + \ldots + \frac{1}{Q_n}. \tag{2.8}$$

2.1 Air damping

Air damping has a few manifestations. A body that travels through a fluid collides with the molecules of that fluid and transmits some of its energy to those molecules. This impingement causes viscous damping by displacing some of the fluid around the body, commonly referred to as viscous drag, and acoustic radiation by exciting the fluid in a perpendicular direction to the motion. The fluid adjacent to a surface parallel to the direction of motion can cause energy loss by Stoke's damping. One common situation in micromechanical systems is a body moving near a stationary body or surface. A parallel motion of this body produces Couette damping by the fluid in the gap, and a perpendicular motion of this body produces squeeze-film damping. The energy loss due to squeeze-film damping dominates when it exists, as in the case of capacitively driven and sensed MEMS [15-19].

As a plate moves perpendicularly toward a parallel plate a small distance away, it forces air to be pushed out of the gap, causing a damping force, and compresses the air in the gap, causing a spring force. Both forces are calculated by solving the Reynolds equation with a number of assumptions and boundary conditions [20].

The Reynolds equation,

$$12\eta\frac{\partial(Ph)}{\partial t} = \nabla\bullet(h^3 P\nabla P) \quad , \tag{2.9}$$

relates time-dependent pressure, P, to the viscosity of the fluid, η, and the distance, h, between the plates for the squeeze-film case. This equation is valid as long as some assumptions are made: the gap, h, is much smaller than the width or length of the plates, there is no pressure gradient from plate to plate, the gas is ideal, and the system is isothermal. In addition, (2.9) assumes the Reynolds number,

$$RE_D = \frac{\rho U D}{\eta}, \tag{2.10}$$

is much less than 1, where ρ and η are the density and viscosity of the fluid, respectively, U is a characteristic velocity, and D is a characteristic length. The characteristic length and velocity in the case of squeeze-film damping correspond to the velocity of the plate and the length of the gap.

If it is further assumed that the gap is uniform over its entire area and the motion of the plate is small compared to the gap, (2.9) can be simplified to

$$\frac{\partial(Ph)}{\partial t} = \frac{h^3}{12\eta}\left(\frac{1}{2}\nabla^2 P^2\right). \tag{2.11}$$

The pressure function is found by linearizing around an operating point h_0 and P_0, so that

$$h = h_0 + \delta h \tag{2.12}$$

and

$$P = P_0 + \delta P \tag{2.13}$$

where δh and δP are much smaller than h and P, respectively. Setting one edge at zero on the y-axis, as in Figure 2.1, where W is the smaller dimension and L is the larger dimension, the linearized equation is

$$\frac{\partial \hat{p}}{\partial t} = \frac{h_0^2 P_0}{12\eta W^2}\frac{\partial^2 \hat{p}}{\partial \xi^2} - \frac{\dot{h}}{h_0} \tag{2.14}$$

where

$$\hat{p} = \frac{\delta P}{P_0} \tag{2.15}$$

and

$$\xi = \frac{y}{W}. \tag{2.16}$$

FIGURE 2.1 *Squeeze-film dimensions*

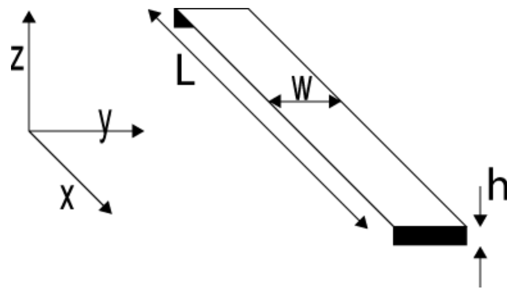

The solution, utilizing eigenfunctions, to an impulse is

$$\hat{p} = -\frac{z_0}{h_0}\sum_{n\ odd}\frac{4}{n\pi}(\sin n\pi\xi)e^{-\alpha_n t}. \tag{2.17}$$

The time-dependent force due to the squeeze-film damping is

$$F(t) = P_0 WL\int_0^L \hat{p}(\xi, t)d\xi \tag{2.18}$$

which yields

$$F(t) = -P_0 WL\frac{z_0}{h_0}\sum_{n\ odd}\frac{8}{n^2\pi^2}e^{-\alpha_n t}. \tag{2.19}$$

If the impulse source, z_0, is generalized, the Laplace transform yields the transfer function form of the force,

$$F(s) = \frac{96\eta LW^3}{\pi^4 h_0^3}z_0\sum_{n\ odd}\frac{1}{n^4}\frac{1}{1+\frac{s}{\alpha_n}}, \tag{2.20}$$

at which point the impulse source can be replaced by a sinusoidal source to produce

$$F(s) = \left[\frac{96\eta LW^3}{\pi^4 h_0^3}z_0\sum_{n\ odd}\frac{1}{n^4}\frac{1}{1+\frac{s}{\alpha_n}}\right]sz(s). \tag{2.21}$$

The summation terms diminish rapidly due to the n^4 and all but the first term can be ignored, yielding

$$F(s) \cong \frac{b}{1+\frac{s}{\omega_c}}sz(s) \tag{2.22}$$

in which the damping constant

$$b = \frac{96\eta L W^3}{\pi^4 h_0^3} \tag{2.23}$$

and the cutoff frequency

$$\omega_c = \frac{\pi^2 h_0^2 P_0}{12\eta W^2}. \tag{2.24}$$

As is shown, the damping force is proportional to the damping constant and the velocity of motion. A spring force also results from the motion of the plate due to the compression of the gas in the gap. The cutoff frequency specifies the size of the squeeze-film spring constant as

$$C = \frac{1}{b\omega_c} \tag{2.25}$$

and depicts the relative importance of the spring force to the damping force. When the frequency of motion is above the cutoff frequency, the spring force will be larger. A typical value for the cutoff frequency is 300 MHz.

At pressures near atmosphere, the viscosity η is not a function of pressure, but when the mean-free path of the air is comparable to the size of the squeeze-film gap, a dependence is seen [21]. A good and simple approximation of this function is

$$\eta = \frac{\eta_{atm}}{1 + 9.638 K_n^{1.159}} \tag{2.26}$$

where

$$K_n = \frac{\lambda}{h_0} = \frac{P_n \lambda_n}{P_0 h_0} \tag{2.27}$$

and λ is the mean-free path of air at the operating pressure, λ_n is the mean-free path of air at a known pressure P_n, and P_0, as before, is the operating pressure.

This analysis is accurate for plates that are much larger than the gap. In order to alleviate inaccuracies due to a small plate, such as in the resonators described in Chapter 3, a correction factor produces effective width and length [22]

$$W_{eff} = W + g(0.8792 + 0.01w) \tag{2.28}$$

and

$$L_{eff} = L + g(0.8792 + 0.01L)\,. \tag{2.29}$$

By combining (2.4) and (2.6) with (2.23), (2.26), and (2.27), we arrive at the equation for the quality factor due to squeeze-film damping:

$$Q_{sq} = \frac{(1 + 9.638K_n^{1.159})\pi^4 h_0^3 m_{eff}\omega_0}{96\eta_{atm}L_{eff}W_{eff}^3}\,. \tag{2.30}$$

The quality factor of the TSMC cantilever (see Chapter 3) due to squeeze-film damping as a function of air pressure is shown as the dotted curve in Figure 2.2. All relevant geometrical values are in Table 3.3.

The surfaces of the resonator that are parallel to the direction of motion also experience viscous damping in the form of Stoke's flow [15]. The damping coefficient of the drag force caused by the lateral motion is

$$b = A\sqrt{\frac{\omega_0\rho\eta_{atm}}{2}}\,, \tag{2.31}$$

FIGURE 2.2 *Simulated air damping quality factor for the TSMC cantilever; dotted line: contribution from squeeze-film damping, dashed line: contribution from Stoke's damping, solid line: total air damping quality factor*

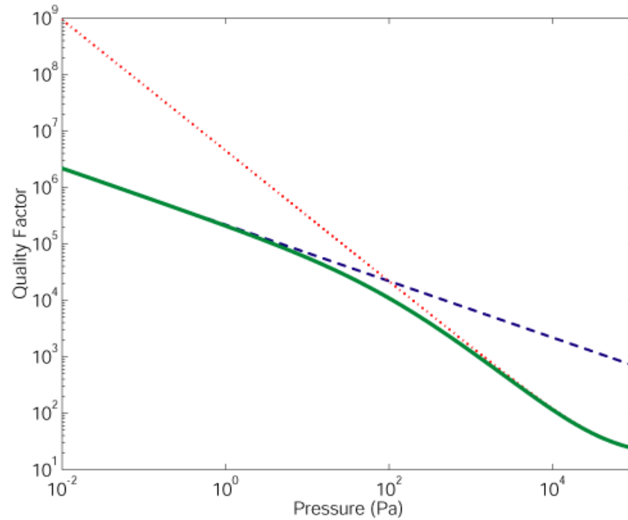

where A is the area of the top and bottom surfaces of the resonator and ρ is the density of air, which is a function of pressure:

$$\rho = P_0 \frac{M}{RT}, \tag{2.32}$$

where M is the molar mass of air (28.96 g/mol), R is the ideal gas constant (8.3145 J/mol-K), and T is the operating temperature.

Since Stoke's damping occurs along the entire length of the beam, and the velocity varies from the anchor to the end, an effective damping coefficient is needed for the

lumped modeling. In a similar calculation to effective mass (see Appendix A), effective Stoke’s damping is

$$b_{eff} = 2\alpha b \tag{2.33}$$

and α is defined in (A.14). Combining (2.33) with (2.4) and (2.6), with both effective mass and effective damping for m and b, respectively, shows that α cancels out and

$$Q = \frac{\omega_0 m}{2b}. \tag{2.34}$$

The Stoke’s damping quality factor is then

$$Q_{st} = \frac{m}{A}\sqrt{\frac{\omega_0 RT}{2PM\eta_{atm}}}. \tag{2.35}$$

The quality factor due to Stoke’s damping is shown in Figure 2.2 along with the squeeze-film quality factor and the total air damping quality factor,

$$Q_{air} = \frac{1}{\dfrac{1}{\dfrac{(1+9.638K_n^{1.159})\pi^4 h_0^3 m_{eff}\omega_0}{96\eta_{atm}LW^3}} + \dfrac{1}{\dfrac{m}{A}\sqrt{\dfrac{\omega_0 RT}{2PM\eta_{atm}}}}} \tag{2.36}$$

obtained with (2.8). As illustrated by Figure 2.2 and (2.36), Stoke’s damping for the TSMC cantilever is small compared to squeeze-film damping for pressures above 100 Pa.

2.2 Acoustic anchor loss

The second dominant energy loss mechanism is acoustic anchor loss. Every resonator is somehow attached to the rest of the chip, and that attachment creates a path for radiation of acoustic energy away from the resonator. Sound waves are created when the anchor moves, sending an internal pressure wave out to the bulk. These acoustic waves can be longitudinal or transverse, depending on the vibrational mode of the resonator and anchor attachment.

Clever design allows the removal of the coupling between the resonator and its anchor to reduce this energy loss by reducing anchor motion [3,23-25]. This design is exemplified by the keys of a xylophone. When the free bar flexes in the fundamental mode, there are two places that have no translational motion – otherwise known as the node points. The vibrating elements are suspended not at the ends, but at these node points. By simply supporting the bar at those points, motional coupling is minimized; thus acoustic radiation is minimized. In addition, higher order modes will have node points at different places, which means the supports will dampen out those modes quickly. This allows the xylophone to have a sustained, pure tonal sound. A similar design can minimize energy loss due to acoustic radiation through the anchor in microresonators, although creating a simple support for a micromechanical beam is difficult. A perfect simple support has infinitesimally small width and exact position at the nodes. With very narrow resonators, it is difficult to make the support beams

much smaller, and the position will have error due to mask bloat, mask misalignment, and lithography limits.

A study of acoustic radiation in terms of transmission phenomena also leads to energy loss minimization. When the acoustic waves created by the vibration of the resonator have a wavelength comparable or smaller than the anchor, the anchor can be modeled as an acoustic transmission line [3]. Just as in an electrical system, the acoustic impedance of a transmission line can be matched to its load to maximize energy transfer. It can also be designed to minimize energy transfer, as in an open or short circuit in the electrical analog.

A vibrating beam can be modeled as a mechanical transmission line. Whereas in the electrical domain, impedance is voltage divided by current, in the mechanical domain impedance is defined as force divided by velocity. By deriving the relationship between force and velocity of a beam, impedance analysis can be done, as in Figure 2.3 for the transverse vibration of a cantilever [26]. By designing the impedance seen looking into the port in Figure 2.3(c) as zero at resonance, the beam's free end has no relationship with the anchor. In other words, assuming the velocity at the anchor is zero, no energy loss will occur due to anchor coupling. The impedances in Figure 2.3(c) for a cantilever beam are

$$Z_a = C\left(\frac{\alpha H_6 + H_1}{H_3}\right), \tag{2.37}$$

FIGURE 2.3 *Equivalent circuit for bending vibration, (a.) cantilever beam, (b.) two-port model, (c.) mechanical impedance model*

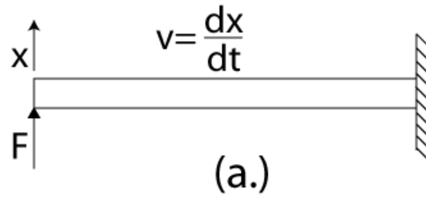

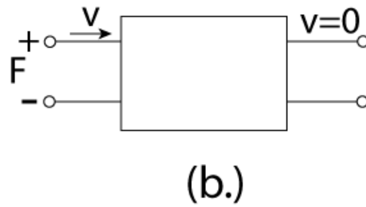

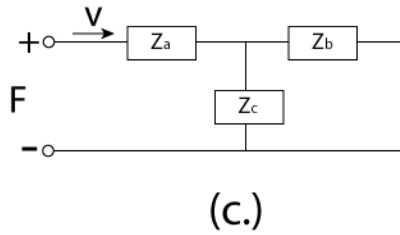

$$Z_b = C\left(\frac{\alpha H_1 - H_5}{\alpha H_3}\right), \tag{2.38}$$

and

$$Z_c = C\left(-\frac{H_1}{H_3}\right), \tag{2.39}$$

where

$$H_1 = \sinh(\alpha)\sin(\alpha), \tag{2.40}$$

$$H_3 = \cosh(\alpha)\cos(\alpha) - 1 \ , \tag{2.41}$$

$$H_5 = \sinh(\alpha)\cos(\alpha) - \cosh(\alpha)\sin(\alpha) , \tag{2.42}$$

$$H_6 = \sinh(\alpha)\cos(\alpha) + \cosh(\alpha)\sin(\alpha) , \tag{2.43}$$

$$C = \frac{j}{L}\sqrt{\rho whEI} , \tag{2.44}$$

and

$$\alpha^4 = \frac{\rho wh}{EI}\omega_0^2 L^4 , \tag{2.45}$$

where L is beam length, ρ is mass density, E is Young's modulus, w is beam width, h is beam thickness, I is the moment of inertia, and ω_0 is the angular resonant frequency of the resonator.

Substituting (2.40), (2.41), (2.42), (2.43), and (2.44) into (2.37), (2.38), and(2.39), and solving for

$$Z_a + Z_b \parallel Z_c = 0 \tag{2.46}$$

the resulting constraint is

$$\cosh(\alpha)\cos(\alpha) + 1 = 0 . \tag{2.47}$$

Numerically solving (2.47) for α yields 1.875, corresponding to the fundamental, 4.694, corresponding to the second mode, and so on. Using the fundamental value will allow the shortest coupling beam. Substituting that value into (2.45), along with the geometrical and material parameters, yields the beam length required to decouple the anchor. A typical laterally-moving beam with width 1 μm, thickness 3.4 μm,

Young's modulus 60 GPa, mass density 2400 kg/m^3, and supporting a resonator with resonant frequency of 1 MHz is designed to be 28.4 μm long to minimize anchor coupling for the cantilever tuning fork topology. This value is commonly referred to as the quarter-wavelength due to the fact that it is one-quarter of the wavelength of the vibration.

This vibrational impedance method is generalized to include all end conditions and locations of force application for a transversely vibrating bar in [26].

2.3 Thermoelastic damping

When a beam bends, it produces a stress gradient in the direction of the bending, which is accompanied by a strain gradient. One side of the beam will be in compression and the other in tension. Volume changes will exist that are opposite on each side of the beam. This volume change will create a difference in temperature. When this temperature gradient is created, the body will move back to thermal equilibrium, and dissipative heat flow will ensue [27-30].

The cyclic energy loss caused by thermoelastic heat flow is a function of the frequency of motion and is avoidable as a dominant contributor to quality factor. The thermoelastic damping factor,

$$\zeta = \Gamma(T)\Omega(\omega), \tag{2.48}$$

is broken into two parts: a temperature-dependent part

$$\Gamma(T) = \frac{\alpha^2 TE}{4\rho C_P} \tag{2.49}$$

and a frequency-dependent part.

$$\Omega(f) = 2\left(\frac{\omega_0\omega}{\omega_0^2 + \omega^2}\right) \tag{2.50}$$

where α is the thermal expansion coefficient, E is Young's modulus, ρ is the density of the material, C_P is the heat capacity of the material at constant pressure, and ω_0 is the characteristic thermoelastic damping frequency,

$$\omega_0 = \frac{\pi^2\kappa}{\rho C_P w^2}, \tag{2.51}$$

where κ is thermal conductivity and w is the width of the beam.

Combining (2.48), (2.49), (2.50), and (2.51) with (2.6), we find the quality factor due to thermoelastic damping to be

$$Q_{te} = \frac{\pi^4\kappa^2 + \omega^2\rho^2 C_P^2 w^4}{\pi^2 w^2 \alpha^2 TE\kappa\omega}. \tag{2.52}$$

Using the material property values in Table 2.1 [31], the thermoelastic quality factor is plotted for constant width and for constant frequency in Figure 2.4 and Figure 2.5 respectively. Since CMOS-MEMS beams are composed of stacks of aluminum and silicon dioxide [5], there will be separate contributions to thermoelastic damping

TABLE 2.1 *Thermal and mechanical properties of aluminum and silicon dioxide*

Property	Al	SiO_2
α (m/m-K)	24×10^{-6}	$.4 \times 10^{-6}$
E (GPa)	68	70
ρ (kg/m^3)	2700	2200
C_P (J/g-K)	.9	.7
κ (W/m-K)	210	1.4

FIGURE 2.4 *Thermoelastic quality factor as a function of frequency (w=1μm); solid line: silicon dioxide, dashed line: aluminum*

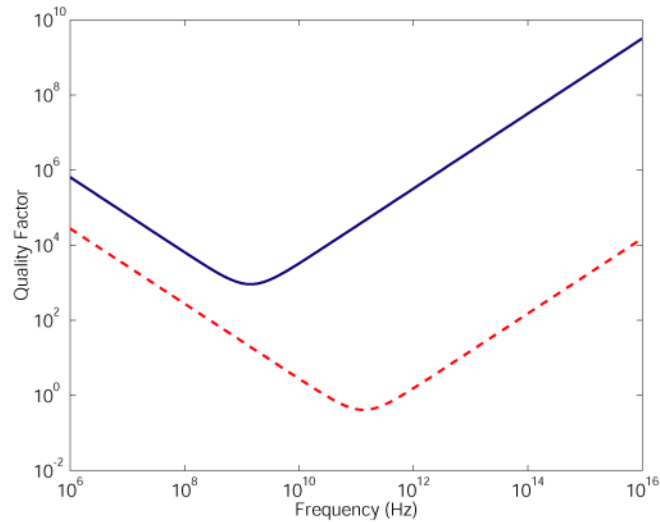

from each material. As Figure 2.4 shows, there is a characteristic frequency for thermoelastic damping, at which quality factor is at the minimum level. The characteristic frequency corresponds to the inverse of the time necessary for an induced thermal

FIGURE 2.5 *Thermoelastic quality factor as a function of beam width (f=1 MHz); solid line: silicon dioxide, dashed line: aluminum*

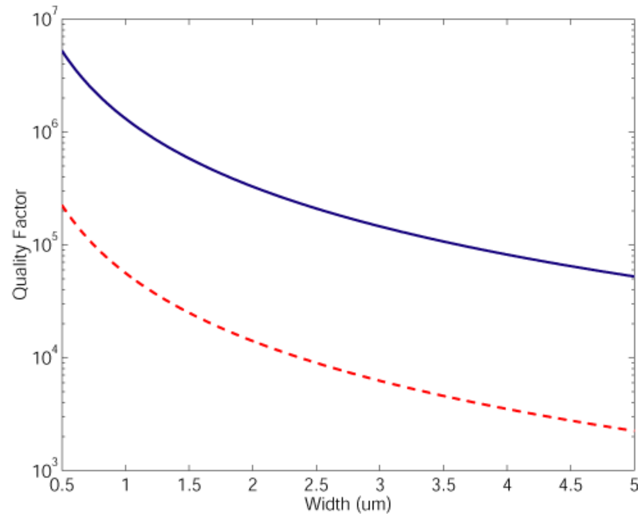

gradient to go to equilibrium within the beam. The goal in designing to minimize thermoelastic damping is to design away from that characteristic frequency, mainly by adjusting the width of the beam. This is easy with small beams in the CMOS-MEMS process, as the characteristic frequencies for aluminum and silicon dioxide are much higher than resonant frequencies that can be designed. Figure 2.5 shows that a beam would have to be wider than a few microns for thermoelastic damping to be dominant.

The characteristic frequencies for both aluminum and silicon dioxide are much higher than the resonant frequencies of the beam resonators studied here. The resulting qual-

ity factors due to thermoelastic damping are much higher than those due to air damping and anchor acoutic loss in the entire design space of this work, and can be neglected.

2.4 Internal losses

The least dominant but ever-present source of energy loss in microresonators is internal friction [32-36]. This source is the hardest to quantify, since it is dependent on the imperfections in the structures of the materials used and is highly dependent on fabrication methods. Internal friction is the dissipation in the form of heat occuring when chemical bonds are made and broken. In a single-crystal beam, point defects and dislocations are the cause of internal friction. The energy loss due to a single defect or dislocation can be modeled and a number of each can be estimated using probabilities to compute the overall internal friction. In a polycrystalline material, the dominant cause of internal friction is grain boundaries. In an amorphous material, the friction is a bulk property, and is greater than the other two cases. In addition, the surface state of a material can cause energy loss due to the fact that there are dangling bonds at the edge of a crystal . Composite materials also have energy loss at the boundary between two layers.

3 Resonator Design

This chapter describes the devices created to experimentally verify energy loss mechanisms. Resonators are designed to test the air damping theory from the previous chapter, and to demonstrate a reduction in anchor loss by tuning fork and quarter-wavelength anchor design methods. The next chapter discusses the system and methods of testing, as well as the results obtained.

The resonators studied are simple beams with electrostatic actuation and capacitive sensing. The input and output electrodes are approximated by parallel plate capacitors, for which the capacitance is accurate for motion that is small relative to the gap size. Several resonators, with different topologies and sizes, are designed on a test chips with interfacing circuitry and wire-bond pads. The basic topologies are the cantilever, or fixed-free beam, and the fixed-fixed beam. In the design for better quality factor, the tuning fork and the free-free beam are explored. Further design discussion focuses on gain, which is related to capacitive sensitivity.

3.1 Chip Design

The CMOS-MEMS process used here allows the layout of many devices on a single chip. Most of the devices on any chip that is entirely composed of test resonators do not work for many design and fabrication reasons. But a low yield on a chip with many devices still produces a few testable resonators, which are described in this chapter.

The two chips studied here were fabricated in the TSMC 0.35 μm 4-metal process [37] and the Jazz SiGe 0.35 μm 4-metal process [38]. The chips are shown in Figures 3.1 and 3.2. Both chips include differential pairs of resonators with differential amplifiers, which are discussed in Chapter 4.

The TSMC chip has a single row of resonators with bond pads for drive signal, differential DC biases, a local oscillator for devices with split-electrode beams, a power supply and current bias for the amplifier, and two differential outputs. All pads except the outputs are in groups and connect to three differential resonator pairs. Table 3.1 lists the resonators on the TSMC chip. Only one device, a cantilever (number 6) is

FIGURE 3.1 *TSMC test chip "actuators77a" (a.) layout (b.) optical microscope image*

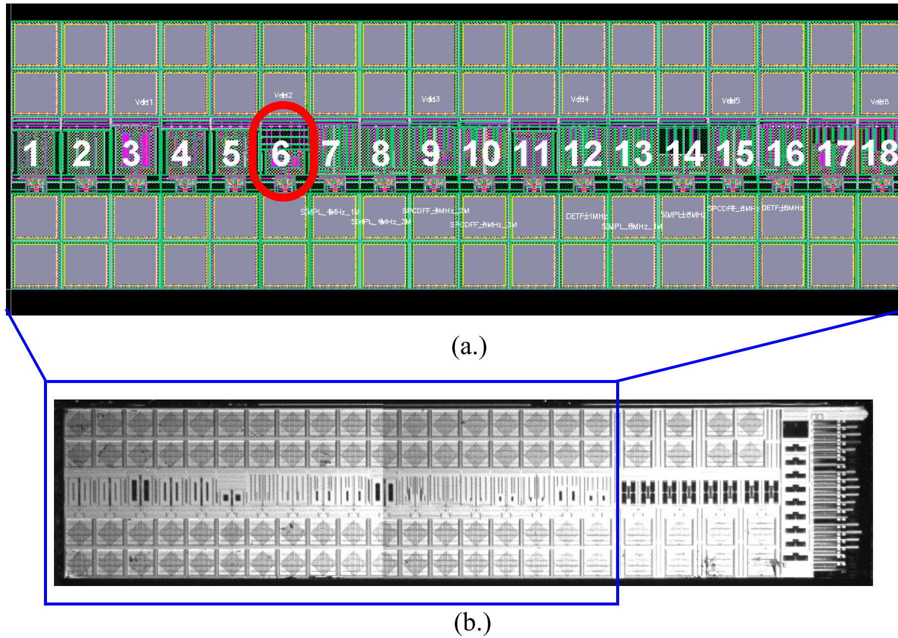

studied here. The square mentioned in the table is used to reduce direct feedthrough and will be explained later.

The Jazz chip has two rows of resonators, each with two output pads. All other pads are connected to each of the resonator pairs on the chip. Table 3.2 lists the resonators on the Jazz chip. Five devices on this chip are studied: the cantilever (number 13), the

FIGURE 3.2 *Jazz test chip "jz60_002" (a.) layout (b.) optical microscope image*

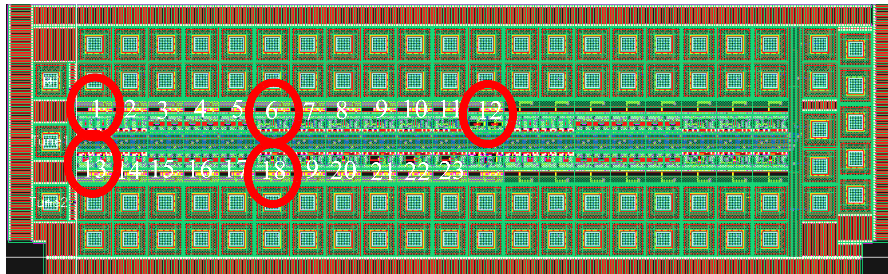

(a.)

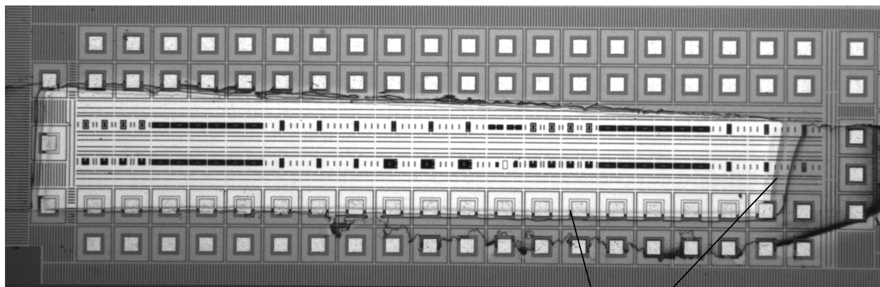

(b.)

TABLE 3.1 *Resonators on the TSMC chip (numbers are shown in Figure 3.1)*

#	Length	Width	Resonator Description	Number of Metal Layers
1	119 μm	1 μm	fixed-fixed beam, no square	2
2	119 μm	1 μm	fixed-fixed beam, no square	3
3	129 μm	1 μm	cantilever with square	2
4	122 μm	1 μm	fixed-fixed beam with square	2
5	122 μm	1 μm	fixed-fixed beam with square	3
6	**32.3 μm**	**1 μm**	**cantilever with square**	**2**
7	59.3 μm	0.5 μm	fixed-fixed beam, no square	1
8	64.9 μm	0.6 μm	fixed-fixed beam, no square	3
9	64.9 μm	0.6 μm	fixed-fixed beam with square	2
10	64.9 μm	0.6 μm	fixed-fixed beam with square	3
11	105.5 μm	0.6 μm	cantilever with square	2
12	55.6 μm	0.6 μm	fixed-fixed tuning fork, no square	2
13	20.95 μm	0.5 μm	fixed-fixed beam, no square	1
14	22.95 μm	0.6 μm	fixed-fixed beam, no square	3
15	29 μm	0.6 μm	fixed-fixed beam with square	2
16	19 μm	0.6 μm	fixed-fixed tuning fork, no square	2
17	55.6 μm	0.6 μm	two electrostatically coupled fixed-fixed tuning forks, no square	2
18	23 μm	0.6 μm	two electrostatically coupled fixed-fixed tuning forks, no square	2

TABLE 3.2 *Resonators on the Jazz chip (numbers are shown in Figure 3.2)*

#	Length	Width	Resonator Description	Number of Metal Layers
1	**27.4 μm**	**1 μm**	**fixed-fixed beam with square**	**3**
2	27.4 μm	1 μm	fixed-fixed beam with square, anchor fillets	3
3 - 5	29.4 μm	1 μm	fixed-fixed beam on snap-in platform (varying final gap sizes)	3
6 - 11	**27.4 μm**	**1 μm**	**fixed-fixed tuning fork with square (varying anchor widths)**	**3**
12	**36.6 μm**	**1.5 μm**	**free-free beam, no square**	**3**
13	**11.4 μm**	**1 μm**	**cantilever with square**	**3**
14	11.4 μm	1 μm	cantilever with square, anchor fillets	3
15 - 17	29.4 μm	1 μm	fixed-fixed beam on snap-in platform (varying final gap sizes)	3
18 - 20	**11.4 μm**	**1 μm**	**cantilever tuning forks with square, quarter-wavelength anchor**	**3**
21 - 23	11.4 μm	1 μm	cantilever tuning forks with square, half-wavelength anchor	3

fixed-fixed beam (number 1), the cantilever tuning fork (number 18), the fixed fixed tuning fork (number 6), and the free-free beam (number 12). The light part in the middle of the chip has been etched, and the dark part on the outside has not. The chip was covered with Kapton tape to mask the parts that did not need to be etched. Having less exposed metal may have helped the etching in the small gaps.

3.2 Basic Topologies

3.2.1 Cantilever

The cantilever topology is the simplest in terms of calculation of resonant frequency. The first cantilever fabricated, in the TSMC process, is described in Table 3.3 and shown in Figure 3.3. The left side gap is for the electrostatic drive and the right side gap is for the capacitive motion sensing.

The square head on the end of the cantilever is designed to reduce direct feedthrough. Direct feedthrough (more fully explained in Chapter 4) is created by a capacitive path from the input drive electrode to the output sense electrode, and produces a current in parallel with the resonator's motional current. This capacitor, like all others, is large when the electrodes are closer together. Therefore, in design it is desirable to separate the drive electrode from the sense electrode. The square is a frame rather than a solid so that there is a smaller additional mass and the resonant frequency is reduced less.

The second cantilever, in the Jazz process, is described in Table 3.4 and shown in Figure 3.4. The Jazz resonators have stepped sidewalls (see Section 3.5), so that metal

3 is 0.4 μm wider than metal 2, which is 0.4 μm wider than metal 1. This "stepping" is also done on the static side of the gap. All beam and gap widths given for the Jazz resonators are averages of all widths. The gap capacitance is calculated without considering fringing fields. The derivation of resonant frequency given in the table is in Appendix A.

TABLE 3.3 *Intended and measured properties of TSMC cantilever*

Property	Layout	Measured	Calculated from Measurements
length	32.3 μm	32.1 μm	
width	1 μm	1.35 μm	
head length	7 μm	7.36 μm	
head width	7 μm	7.36 μm	
head beam width	1 μm	1.28 μm	
thickness	3.4 μm	3.28 μm	
drive gap width	1.5 μm	1.41 μm	
sense gap width	1.55 μm	1.19 μm	
drive capacitance	53.9 aF		58.7 aF
sense capacitance	52.2 aF		69.5 aF
effective mass	244 pg		306 pg
spring constant	1.11 N/m		2.64 N/m
resonant frequency	340 kHz	510 kHz	467 kHz

The TSMC cantilever has a single-conductor beam, which means the DC bias on both the input and output gaps are controlled by one source. All Jazz resonators are split-conductor beams, allowing independent control of the input and output biases. A

FIGURE 3.3 *TSMC cantilever (a.) diagram (b.) scanning-electron micrograph*

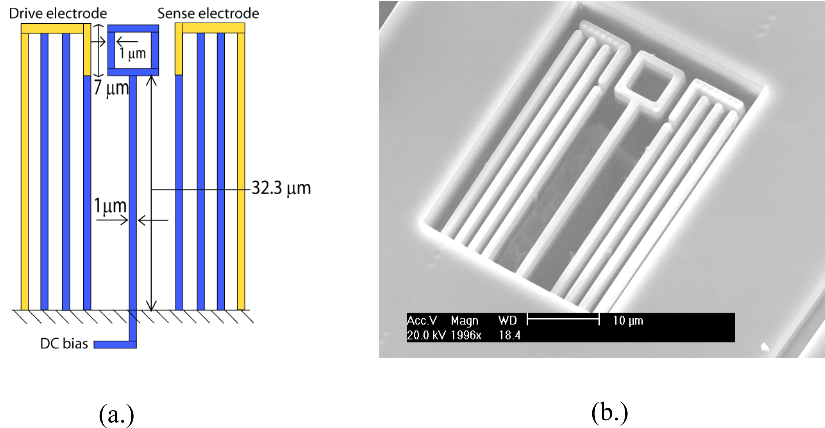

(a.) (b.)

split-conductor beam also improves mixing, as the input side of the beam can have only a local oscillator (LO) signal and the output side of the beam can have only a DC bias. This situation reduces unwanted frequency components in the output due to interactions of the LO on the output gap.

Due to residual stress gradients in the deposited thin films, released cantilevers will curl up. The curl decreases with thickness. The 2 metal layer TSMC cantilever displaces about .6 μm at the end, and the 3 metal layer Jazz cantilever displaces about .4 μm at the end. The stress gradient, and thus the curl, can be reversed or eliminated by using different materials, but the CMOS processes discussed here are not flexible. If a cantilever resonator is designed with stator electrodes that are not released, the electrodes will not line up vertically, and the capacitance will be severely decreased. To

TABLE 3.4 *Intended and measured properties of Jazz cantilever*

Property	Layout	Measured	Calculated from Measurements
length (not including head)	11.4 µm	10 µm	
width	1 µm	1.3 µm	
head length	7 µm	7.4 µm	
head width	7 µm	7.3 µm	
head beam width	1 µm	1.3 µm	
thickness	5.03 µm	4.99 µm	
drive gap width	1.2 µm	1.2 µm	
sense gap width	1.2 µm	1.2 µm	
drive capacitance	118 aF		103 aF
sense capacitance	118 aF		103 aF
effective mass	326 pg		432 pg
spring constant	22.8 N/m		64.0 N/m
resonant frequency	1.33 MHz	2.29 MHz	1.94 MHz

FIGURE 3.4 *Jazz cantilever (a.) diagram (b.) scanning-electron micrograph*

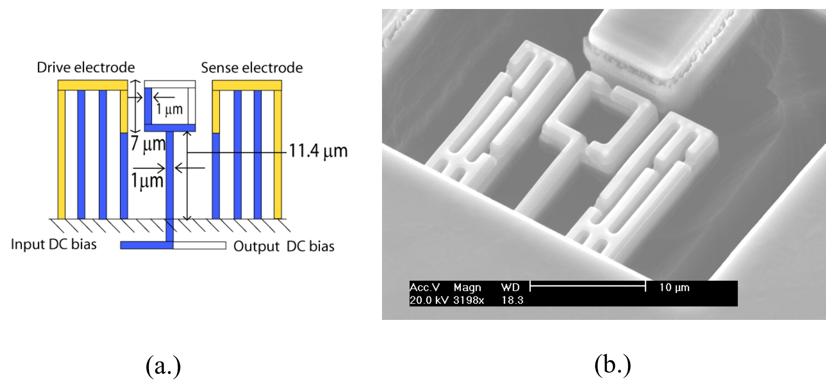

(a.) (b.)

fix this problem, curl-matched electrodes, such as in Figures 3.3 and 3.4, are designed to curl the same amount as the beam. The amount of curl is a weak function of width, so the curl-matched electrodes are composed of several beams of the same width as the resonator connected with a few perpendicular beams to make them stiff. Making the released electrodes much stiffer than the cantilever is essential to avoid vibration of the electrode.

3.2.2 Fixed-fixed beam

The fixed-fixed, or clamped-clamped, beam is stiffer than the cantilever due to anchors at both ends. It can be used to make a resonator with a higher resonant frequency without making features too small to be fabricated. The fixed-fixed beam in the Jazz process is described in Table 3.5 and shown in Figure 3.5.

TABLE 3.5 *Intended and measured properties of Jazz fixed-fixed beam*

Property	Layout	Measured	Calculated from measurements
length (including head)	27.4 μm	25.7 μm	
width	1 μm	1.3 μm	
head length	7 μm	7.6 μm	
head width	7 μm	7.6 μm	
head beam width	1 μm	1.3 μm	
thickness	5.03 μm	4.99 μm	
drive gap width	1.2 μm	1 μm	
sense gap width	1.2 μm	1 μm	
drive capacitance	118 aF		127 aF
sense capacitance	118 aF		127 aF
effective mass	347 pg		468 pg
spring constant	235 N/m		285 N/m
resonant frequency	4.13 MHz	1.57 MHz	6.19 MHz

CMOS processes leave residual stress in the metal and oxide layers which must be relieved in order to avoid a frequency shift. A cantilever relieves that stress as soon as it is released by extending and curling. A fixed-fixed beam can not relieve the stress in the same way, so it is designed into a platform, which allows stress relief in the direction of the beam length, as shown in Figure 3.5(b).

FIGURE 3.5 *Jazz fixed-fixed beam (a.) diagram (b.) scanning-electron micrograph*

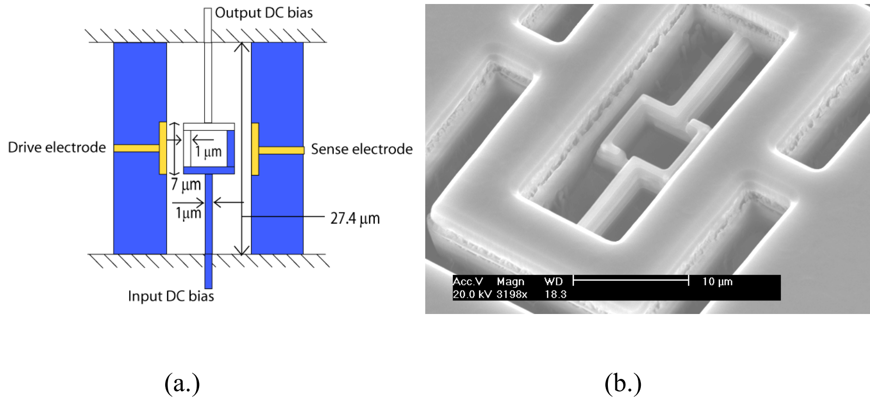

(a.) (b.)

3.3 Design for Resonant Frequency

From (2.3) and (2.4), the resonant frequency for a second-order mechanical system is

$$f_r = \frac{1}{2\pi}\sqrt{\frac{k}{m}}, \tag{3.1}$$

where k is mechanical stiffness and m is mass. A stiffer beam will have a higher resonant frequency, and a more massive beam will have a lower resonant frequency. Usually, k and m are dependent on some of the same geometric variables, so this ratio simplifies. For instance, in the case of a laterally-moving cantilever,

$$k = \frac{Eh}{4}\frac{w^3}{L^3} \tag{3.2}$$

and

$$m = \alpha\rho whL, \tag{3.3}$$

where E is Young's modulus, h is thickness, w is width, L is length, ρ is mass density, and α is an effective mass factor (see Appendix A). The scaling of resonant frequency is

$$f_r = \frac{1}{2\pi}\sqrt{\frac{E}{4\alpha\rho}}\frac{w}{L^2}. \tag{3.4}$$

Young's modulus and density are functions of the materials used and not alterable in the CMOS-MEMS process. Thus, in this example, resonant frequency is directly proportional to width and inversely proportional to the square of the length. As shown in Appendix A, the only geometrical variable that α is dependent on is L. The design of resonant frequency, after the process is set, comes down to two geometric variables.

3.4 Design for Better Quality Factor

3.4.1 Minimization of anchor loss

As stated in Chapter 2, loss through the anchor is due to vibrational coupling from the resonator to the bulk to which it is attached. To reduce this coupling, a tuning fork topology can be used to separate the resonator from the anchor by a coupling beam

which does not vibrate. In addition, a quarter-wavelength coupling beam can reflect the energy back into the resonator.

Tuning fork. A tuning fork resonator is composed of two identical resonator beams connected at their bases by a cross-beam which is connected to the substrate by an anchor beam. Figures 3.6 and 3.7 show cantilever and fixed-fixed tuning forks, respectively, with the dimensions given in Table 3.4 and Table 3.5. The tuning fork is driven antisymmetrically, which ideally causes the motion at the base to cancel out. Since the anchor beam is attached at the base, it will not move, thus there is no anchor coupling. However, any mass imbalance caused by imperfect fabrication will cause coupling.

FIGURE 3.6 *Jazz cantilever tuning fork (a.) diagram (b.) scanning-electron micrograph*

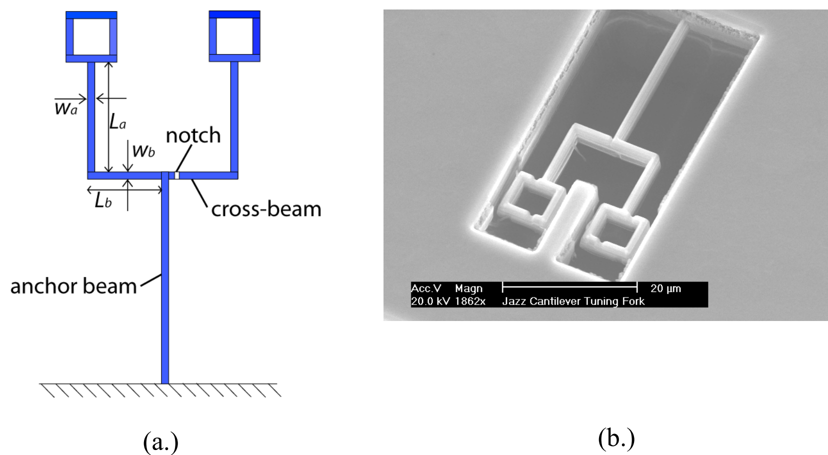

(a.) (b.)

FIGURE 3.7 *Jazz fixed-fixed tuning fork*

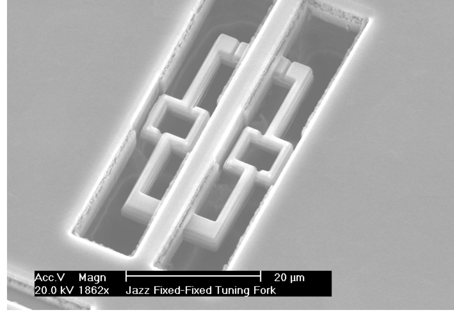

The tuning fork structure is essentially two symmetrical crab-leg resonators, which has a different resonant frequency than the single cantilever. The spring constant for a crab-leg resonator with a cantilevered end, k_{cl}, is [39]

$$k_{cl} = \frac{Eh}{12L_a^2}\frac{1}{\left(\frac{L_a}{3w_a^3} + \frac{L_b}{w_{b^3}}\right)}, \tag{3.5}$$

where L_a, L_b, w_a, and w_b are indicated in Figure 3.6(a). The effective mass (see Appendix A) is

$$m_{eff} = \frac{33}{140}m_a + \frac{1}{5}m_b, \tag{3.6}$$

where m_a and m_b are the mass of the section of length L_a and L_b, respectively. The resonant frequency, utilizing (2.5), is therefore

$$\omega_0 = \sqrt{35}\sqrt{\frac{Ehw_a^3w_b^3}{L_a^2(L_aw_b^3 + 3L_bw_a^3)(33m_a + 28m_b)}}. \tag{3.7}$$

The effect of the width of the cross-beam is seen when the actual dimensions of the cantilever tuning fork are substituted in (3.7) and w_b is varied. Using the dimensions of Table 3.4 for L_a, w_a, and thickness for the masses, and 5.7 µm for the designed dimension of L_b, the resonant frequency as a function of w_b is shown in Figure 3.8.

FIGURE 3.8 *Resonant frequency of cantilever tuning fork with respect to width of the cross-beam*

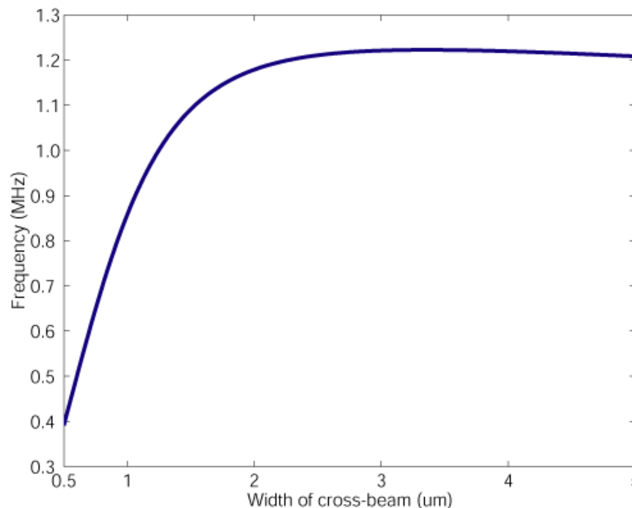

Note that in the figure, as the width approaches the size of the length of the cross-beam, the curve starts to descend slightly. This is because the beam theory used is no longer valid. The exact curve asymptotically reaches the value of the frequency of a single cantilever as the cross-beam approaches the shape of the bulk. The designed

cross-beam width of 1 μm produces a resonant frequency of 859 kHz. Designing it wider would increase the frequency close to that of a single cantilever.

Quarter-wavelength anchor beam. As derived in Chapter 2, a coupling beam whose length is one quarter of the wavelength of vibration provides zero reaction force at resonance. This effectively isolates the resonator from the substrate. The cantilever tuning fork in Figure 3.6 incorporates a quarter-wavelength coupling beam, which is 23.8 μm long and designed for a resonant frequency of 1.43 MHz. This is a design error, as the calculated resonant frequency with designed geometrical parameters of the Jazz cantilever is 1.33 MHz (Table 3.4).

Free-free beam. If a simple beam could be suspended in space without tethers, it would have no anchor coupling, and therefore no energy loss due to an anchor. While this can not be done, it can be approximated closely with a free-free beam. The fundamental mode shape of an untethered beam has two points that do not displace from the original position. Coupling beams that are attached at these points hold the resonator in place, while minimizing anchor coupling. These beams will still rotate at the point of attachment to the resonator so some coupling will still occur, which can itself be minimized with the quarter-wavelength method, producing an achor beam that is 28.3 μm long. A free-free beam in the Jazz process is described in Table 3.6 and shown in Figure 3.9.

TABLE 3.6 *Intended and measured properties of Jazz free-free beam*

Property	Layout	Measured	Calculated from measurements
length	36.6 µm	37.8 µm	
width	1.5 µm	1.8 µm	
thickness	5.03 µm	4.99 µm	
coupling beam length	12.2 µm	11.5 µm	
coupling beam width	1.3 µm	1.4 µm	
coupling beam position from end of resonator (to center)	8.2 µm	8.6 µm	
drive gap width	1.2 µm	.9 µm	
sense gap width	1.2 µm	.8 µm	
drive capacitance	118 aF		130 aF
sense capacitance	118 aF		146 aF
resonant frequency	5.76 MHz	870 kHz	6.47 MHz

The measured resonant frequency of the free-free beam is much lower than the expected frequency. This could be due to compressive stress caused by the anchor beams.

3.5 Design for Gain and Fabrication Issues

The gain of the filter incorporating resonators is

FIGURE 3.9 *Jazz free-free beam (a.) diagram (b.) scanning-electron micrograph*

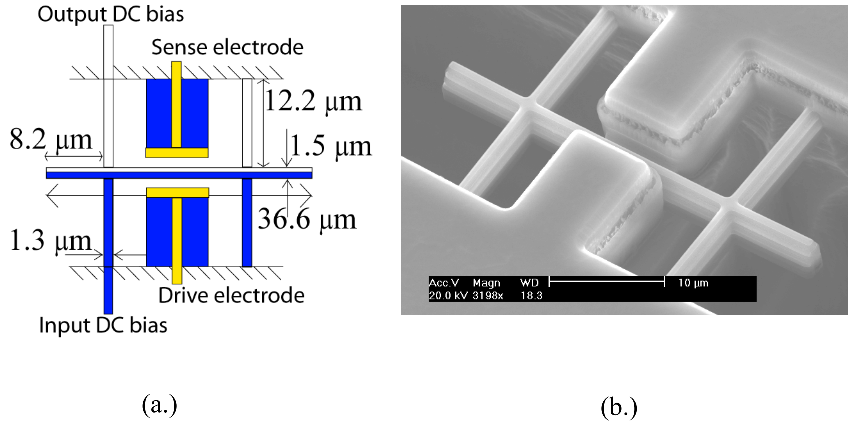

(a.) (b.)

$$\frac{v_{out}}{v_{in}} = \frac{AH\omega_r QV_{DC_{drive}}V_{DC_{sense}}\left(\frac{\partial C}{\partial x}\right)^2}{2k}, \tag{3.8}$$

where A is the voltage gain of the external amplifier, H is the transresistance gain of the on-chip amplifier, which is inversely proportional to frequency, Q is the quality factor, $V_{DCdrive}$ and $V_{DCsense}$ are the DC biases applied to the drive and sense gaps, respectively, k is spring constant, and dC/dx is the capacitive sensitivity. (3.8) assumes that the drive and sense gaps are the same size. When the capacitor comprised of the beam and the stator electrode is approximated as parallel-plate, the capacitive sensitivity is

$$\frac{\partial C}{\partial x} = \frac{\varepsilon A}{[g - x(t)]^2} \tag{3.9}$$

which, in the small-motion approximation, is

$$\frac{\partial C}{\partial x} = \frac{\varepsilon A}{g^2}, \tag{3.10}$$

where ε is the dielectric constant of air, A is the area of the capacitor, and g is the size of the gap. The two ways to increase capacitive sensitivity are increasing the capacitive area, and decreasing the size of the gap. For laterally-moving beams, increasing the area means making a thicker beam, which is limited in the CMOS-MEMS process to a few discrete levels, or increasing the length of the electrode, which is limited by the size of the beam. Decreasing the gap is limited by design rules of the CMOS process, and futher by the limits of the post-process etches. In practice, a minimum etchable gap size is found and that value is used in all designs, though decreasing the gap remains an area of research. The smallest gap that has been successfully etched repeatably is 1 μm with straight sidewalls, though a 0.8 μm gap at metal 1, which increases by 0.4 μm for metal 2 and again for metal 3 (the gaps for the Jazz resonators, see Figure 3.10), has etched successfully in some instances. Influences in etching success may include amount of the top metal exposed on the chip being etched and the proximity of the top metal to the gap.

To alleviate fabrication problems for small gaps, two methods have been devised: stepping metal layers on sidewalls and creating a actuated snap-in electrode. Stepping back each higher metal layer on a gap edge potentially makes it easier for a vertically anisotropic etch to proceed (Figure 3.10(c.)). The reverse pyramid shape may provide better delivery of reactant species and removal of waste species during the etch. In

addition, this configuration diminishes the effect of misalignment, as shown in Figure 3.10. Shown is a lateral misalignment of 10% of the width of the beam of the

FIGURE 3.10 *Effect of mask misalignment on CMOS-MEMS beam: (a.) designed straight-sidewall beam; (b.) mask misalignment of (a.); (c.) designed stepped-sidewall beam; (d.) misalignment of (c.)*

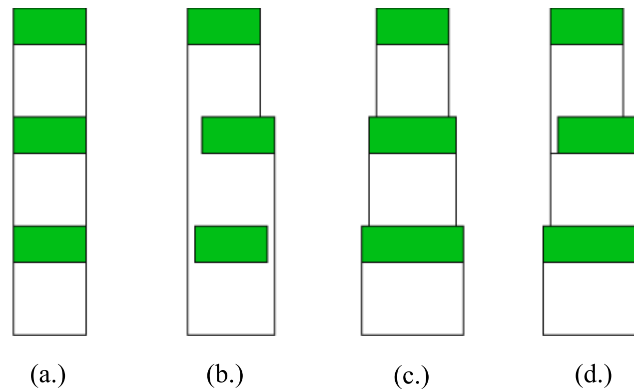

top two metal layers, in opposite directions. The straight-sidewall beam increases in mass by 13% and the center of mass shifts by 5%. The stepped-sidewall beam increases only 2.8% in mass and the center of mass moves by only 1.4%.

The snap-in electrode allows an initially large gap to be etched easily. Then when the beam's DC bias is applied, the platform that the beam is attached to snaps to a position that leaves a small gap [40]. The platform containing the beam is spring-mounted, and the snap-in force is increased by long plates that increase the area of the snap-in capacitor. Figure 3.11 shows the snap-in resonator.

FIGURE 3.11 *Fixed-fixed beam with snap-in electrode*

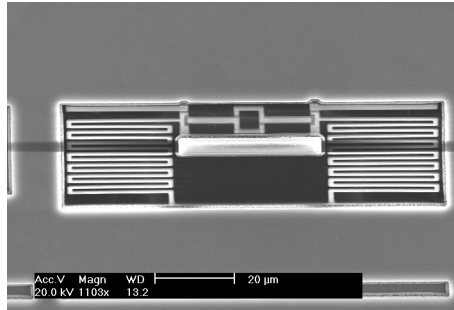

Some beams have been impossible to release due to overly optimistic designed gap sizes and top metal too close to the gap. The silicon dioxide etch coats the sidewalls with a polymer to facilitate vertical etching. If this polymer is too thick, it coats the entire gap and etching stops. To test these beams, the gap was etched out using a focused ion beam (FIB). Before and after SEMs of this microsurgery process are shown in Figure 3.12.

FIGURE 3.12 *Microsurgery gap clearing (a.) Before FIB (b.) After FIB*

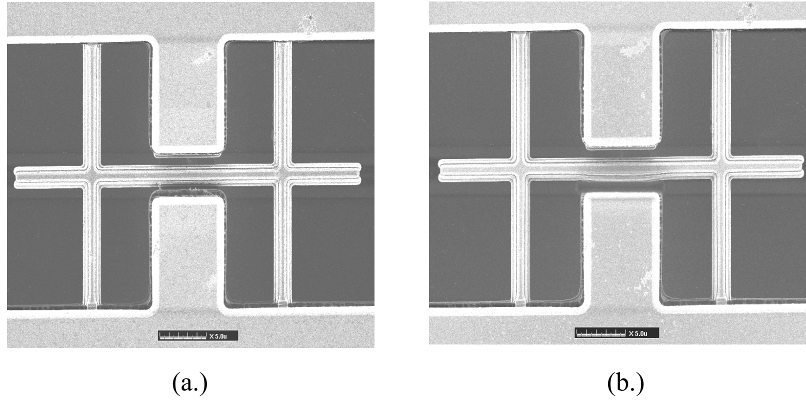

(a.) (b.)

4 Testing and Results

In order to test the theories of energy loss, the resonators described in Chapter 3 were placed in a vacuum testing system. The on-chip amplifier output was routed to an off-chip interface circuit and the resulting signals were sent to a network analyzer. This chapter describes the system that was devised to test the resonators and details the results from those tests.

4.1 On-Chip Amplifier Design

An interface circuit is designed on the same chip as the microresonators. The primary advantage of the CMOS-MEMS process is this ability to integrate MEMS with interface circuitry. All of the described devices use the same circuit topology, although the TSMC and the Jazz amplifiers have different transistor sizes and different gains.

The fully differential amplifier, shown in Figure 4.1, includes a transistor connecting the gate to the drain of each input transistor, which is normally biased in the cutoff

FIGURE 4.1 *Fully differential on-chip amplifier*

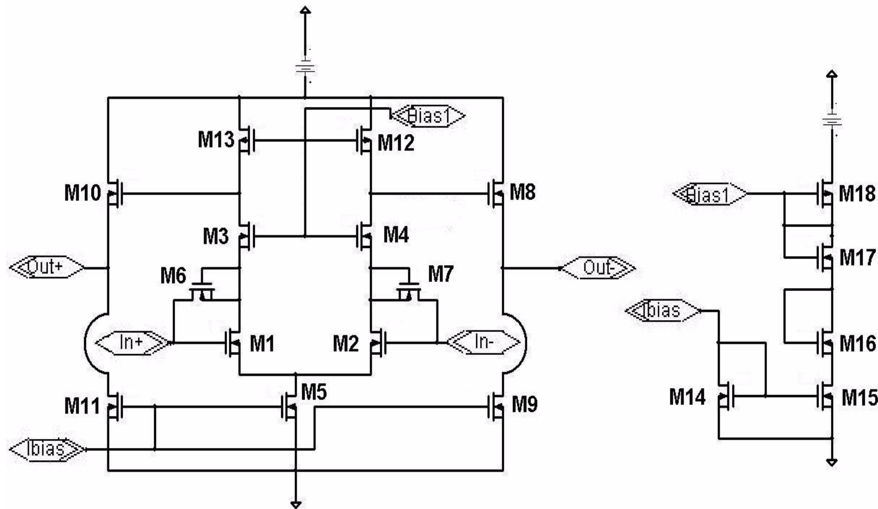

region [41]. This transistor sets the input voltage bias, which is necessary as the inputs are connected only to the high-impedance capactive sense nodes. The amplifier is used to convert a motional current to a voltage. This design uses the parasitic capacitance to ground, C_p, to convert the current to voltage, which is then amplified (Figure 4.2).

Table shows the characteristics of the TSMC and Jazz amplifiers determined with Spectre simulations. Table 4.2 lists the transistor sizes of both amplifiers. The TSMC

FIGURE 4.2 *Differential test system*

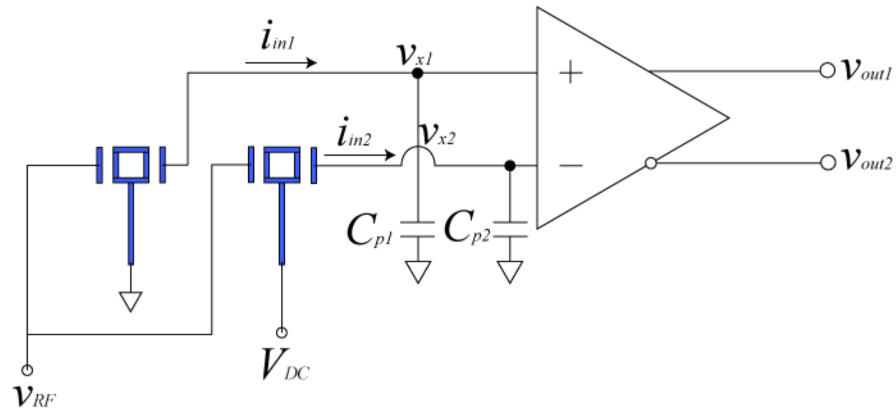

and Jazz amplifiers have the same topology, but the Jazz amplifier has been sized for higher gain.

TABLE 4.1 *Characteristics of the TSMC and Jazz on-chip amplifiers*

Characteristic	TSMC Amplifier	Jazz Amplifier
voltage supply	5 V to GND	3.3 V to GND
voltage gain $(v_{out1}-v_{out2})/(v_{x1}-v_{x2})$	73.4	137
voltage bandwidth	2.1 MHz	10.5 MHz
transimpedance gain $(v_{out1}-v_{out2})/(i_{in1}-i_{in2})$ @ 500 kHz	38.0 MΩ	386 MΩ
transimpedance bandwidth	21 MHz	10.5 MHz

TABLE 4.2 *Transistor sizes for the TSMC and Jazz amplifiers (sizes are given as transistor width / transistor length, in μm)*

Transistor	Type	TSMC	Jazz
M1	N	18/.9	400/.8
M2	N	18/.9	400/.8
M3	N	36/.9	240/.8
M4	N	36/.9	240/.8
M5	N	24/.9	64/.8
M6	N	3/2.7	3/2.7
M7	N	3/2.7	3/2.7
M8	N	40/1.2	16/.8
M9	N	36/.9	32/.8
M10	N	40/1.2	16/.8
M11	N	36/.9	32/.8
M12	P	15/1.2	144/1
M13	P	15/1.2	144/1
M14	N	24/.9	24/.8
M15	N	24/.9	16/.8
M16	N	18/.9	16/.8
M17	N	36/.9	32/.8
M18	P	30/1.2	64/1

Each device is designed as an identical pair of resonators as shown in Figure 4.2. By applying the same signal, v_{RF}, to the drive electrode, the same feedthrough current appears at the input of the differential amplifier as common-mode and is rejected. Driving each resonator with the same drive signal and using opposite DC biases on the beam creates differential motional currents. However, it is impossible to fabricate two resonators with exactly the same resonant frequency, and the difference causes

two peaks that blend together rather than a well-defined single peak. In order to accurately measure quality factor, only one resonator is biased, with V_{DC}, and the other grounded. This produces half the output amplitude from the amplifier, but allows a single well-defined peak.

Characteristics of the TSMC and Jazz on-chip amplifiers

Characteristic	TSMC Amplifier	Jazz Amplifier
voltage supply	5 V to GND	3.3 V to GND
voltage gain $(v_{out1}-v_{out2})/(v_{x1}-v_{x2})$	73.4	137
voltage bandwidth	2.1 MHz	10.5 MHz
transimpedance gain $(v_{out1}-v_{out2})/(i_{in1}-i_{in2})$ @ 500 kHz	38.0 MΩ	386 MΩ
transimpedance bandwidth	21 MHz	10.5 MHz

4.2 Testbed

In order to test the resonators for frequency response, a system was built which includes the released chip along with an external amplifier, interfaces to the instru-

mentation, and a vacuum system which provides not only controlled air pressure, but also a shield from interference. A diagram of the system is shown in Figure 4.3.

FIGURE 4.3 *Diagram of test system*

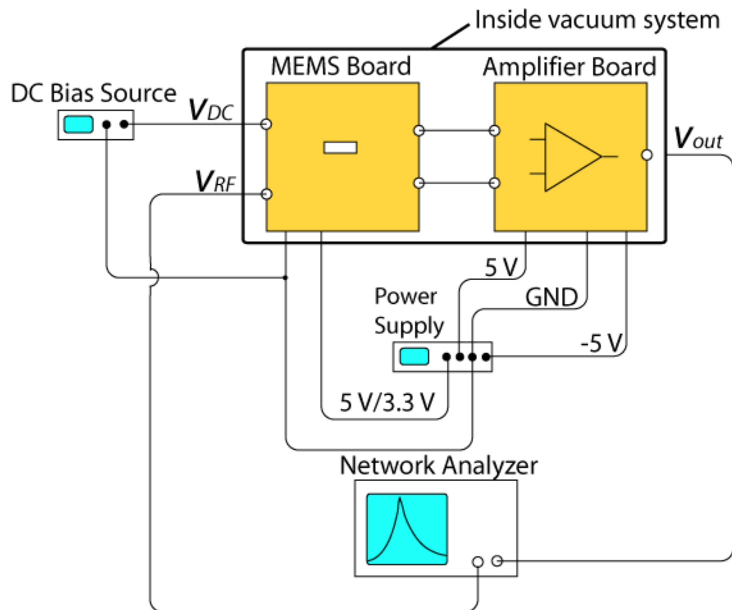

Initial tests were done by wirebonding the chip in a 40-pin dual in-line package (DIP) placed on a breadboard. Due to large amounts of feedthrough caused by the capacitance between leads on the breadboard, a printed circuit board (PCB) was designed (Figure 4.4). Each MEMS chip tested was secured with double-sided tape and wirebonded on a dedicated board. This board connected to other boards and equipment

with coaxial cable BNC jacks for the signal lines and a DB25 connector for the DC lines. It also included a resistor between the V_{DD} power supply line and the I_{BIAS} line to set the current bias into the amplifier. This resistor is 15 kΩ for the TSMC chip, which supplies about 333 μA. The amplifiers on the Jazz chip are all connected to one I_{BIAS} pad, so the resistor chosen was 625 Ω, which supplies 220 μA to each of 24 circuits. In addition, 10 μF bypass capacitors from the V_{DD} and I_{BIAS} lines to ground shunt high-frequency noise.

FIGURE 4.4 *Photograph of MEMS PCB*

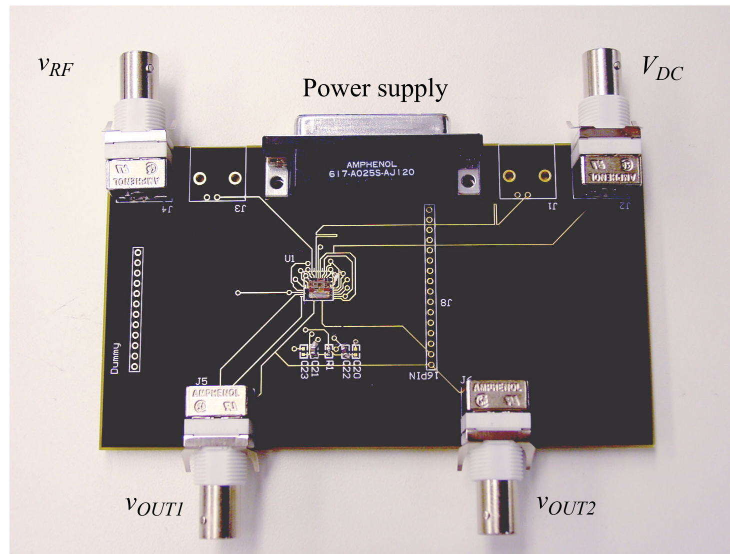

An external amplifier, Figure 4.5, is used to amplify the signal further for testing. This large-bandwidth, low-noise amplifier is a LMH6624 from National Semiconductor. It is surface-mount soldered on a custom-made printed circuit board along with the

input and feedback resistors, as well as BNC connectors for the signal lines and a DB9 for the power supply lines. R1 and R2 are 10 kΩ, R3 and R4 are 240 kΩ, C1 and

FIGURE 4.5 *External amplifier PCB (a.) schematic (b.) photograph*

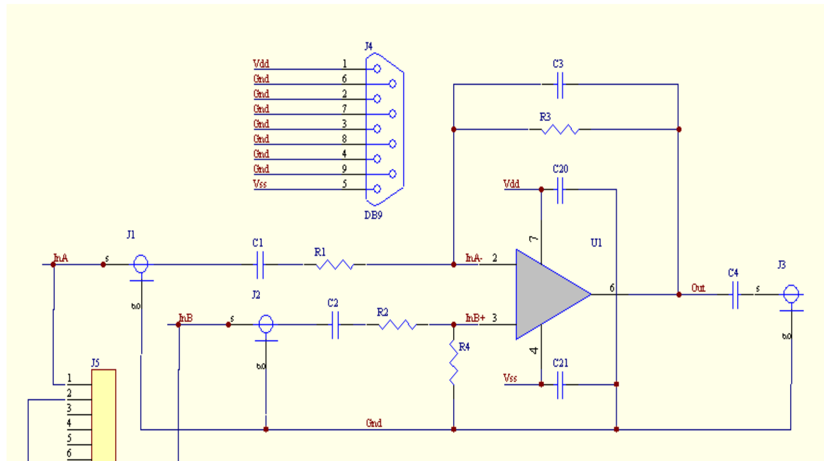

(a.)

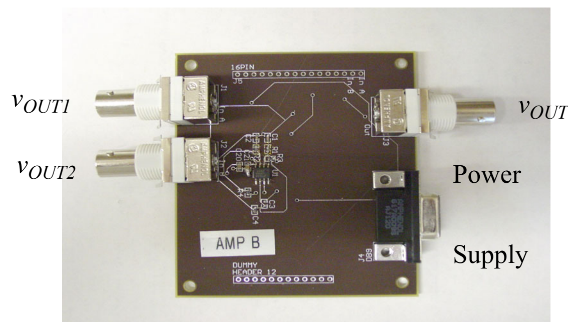

(b.)

C2 are 1 nF, C20 and C21 are 1 µF, C3 is left open and C4 is shorted.

The vacuum system, Figure 4.6(a), is a custom-made metal box connected to a roughing pump. It has coaxial cable throughputs for interfacing signal lines and a DB25 cable throughput for interfacing DC and low-frequency signal lines. The cables from the vacuum system go directly to the network analyzer, DC bias source, and power supply source (Figure 4.6(b)).

FIGURE 4.6 *Testing system (a.) vacuum chamber (b.) test equipment*

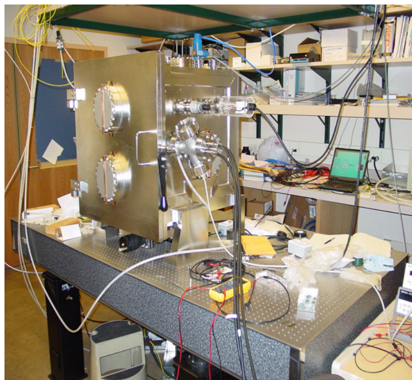

(a.)

(b.)

4.3 Measured Transfer Functions

The network analyzer is used to obtain a dataset in a small range of frequencies around the visible peak. The direct feedthrough is measured by setting the DC bias on the output side of the beam to be the same as the bias on the input node to the circuit.

This will produce a voltage of zero across the gap and no motional current will be detected by the circuit. This voltage has been experimentally found to be about 1.3 V for the Jazz amplifier. In a spreadsheet program, the feedthrough is subtracted from the raw data, yielding a curve corresponding to the motional signal, and the center frequency and 3 dB points are found. The quality factor of each resonator is then calculated from (2.7). For cases in which the motional signal and the feedthrough signal are similar in magnitude, the sum does not produce a symmetrical peak, due to phase interactions. The complex magnitude of both the raw data and the feedthrough are saved as in Figure 4.7. Subtracting the feedthrough from the raw data as complex numbers yields the symmetrical peak seen when the magnitudes of the two signals are significantly different from each other. This procedure was necessary for the fixed-fixed tuning fork and the free-free beam.

Table 4.2 shows the quality factors measured from the six devices described in Chapter 3. The air pressure for all measurements was near 100 mTorr, but v_{DC} was changed for different devices as described. For stiffer beams, it was necessary to increase the DC bias so that the output signal was more visible and farther above the noise. The magnitude of the input signal was 17 mV for the TSMC cantilever and 224 mV for the Jazz resonators, which are stiffer. Increasing the input signal increases the signal-to-noise ratio, producing a cleaner curve. Yet if the visible peak is non-symmetrical, it indicates that the resonator is being driven into the non-linear region. Decreasing the

FIGURE 4.7 *Raw data for fixed-fixed tuning fork: Real and Imag -- with DC bias; F Real and F Imag -- with DC bias = 0 on output gap (feedthrough)*

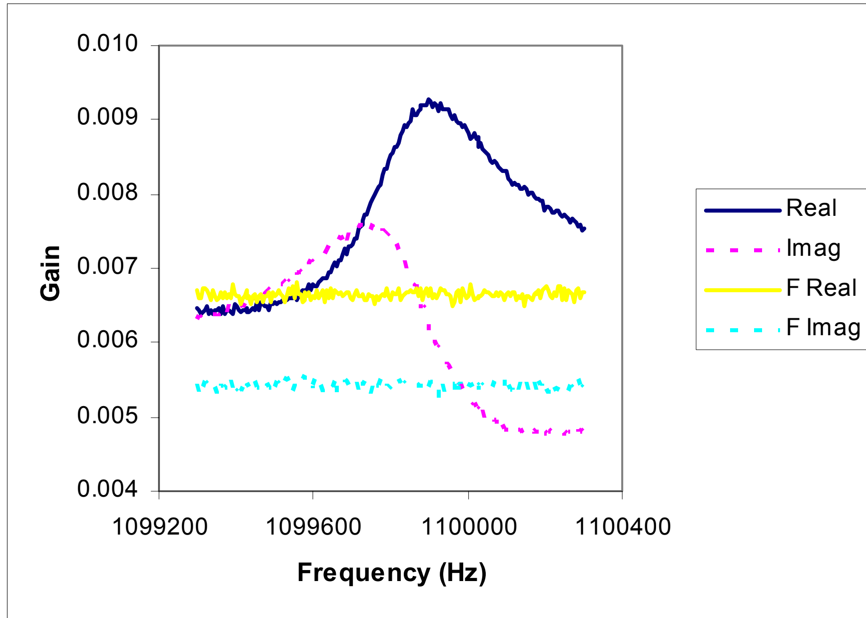

input signal moves it back into the linear region without sacrificing gain (since the network analyzer measures the ratio of the power out of the system, v_{OUT}, to the power into the system, v_{RF}). The measured resonance frequencies and amplitudes at resonance are compared with the expected frequencies and amplitudes in Table 4.3. The calculated amplitude at resonance, x, is

$$x = \frac{FQ}{k}, \tag{4.1}$$

where F is the input force with the input signal amplitude used in testing, Q is the quality factor and k is the spring constant.

TABLE 4.3 *Measured quality factors of each resonator @ 100 mTorr*

Resonator	DC Bias	Quality Factor	Resonant Frequency
TSMC cantilever	+15 V	1480	510 kHz
Jazz cantilever	+12 V	1620	2.29 MHz
Jazz fixed-fixed	+19 V	1046	1.57 MHz
Jazz cantilever tuning fork	+12 V	2010	914 kHz
Jazz fixed-fixed tuning fork	+10 V	2750	1.10 MHz
Jazz free-free	+10 V	1850	870 kHz

TABLE 4.4 *Measured and expected resonant frequency and amplitude at resonance*

Resonator	Measured Resonant Frequency	Calculated Resonant Frequency	Measured Amplitude at Resonance	Calculated Amplitude at Resonance
TSMC cantilever	510 kHz	467 kHz	1.48 μm	4.17 nm
Jazz cantilever	2.29 MHz	1.94 MHz	3.23 nm	2.92 nm
Jazz fixed-fixed beam	1.57 MHz	6.19 MHz	.208 nm	1.37 nm
Jazz cantilever tuning fork	914 kHz	859 kHz	6.22 nm	7.24 nm
Jazz fixed-fixed tuning fork	1.10 MHz	6.19 MHz	.208 nm	1.37 nm
Jazz free-free beam	870 kHz	6.47 MHz	.103 nm	.977 nm

The resonant frequencies of the TMSC and Jazz cantilevers and the Jazz cantilever tuning fork were greater than expected. This is due to either a wider or shorter beam than expected, or mass loading from a polymer byproduct from the RIE etches. The Jazz fixed-fixed beam and the Jazz fixed-fixed tuning fork had a much lower resonant frequency than expected due to compressive stress. These, along with the lowered frequency of the free-free beam, are discussed in Section 4.4.2. The resonant peaks of the six described devices, with feedthrough subtracted, are shown in Figure 4.8. The Jazz fixed-fixed beam graph shows two peaks. Both beams in the differential pair were released and both were biased. The quality factor is measured with the higher

frequency peak and may have an artificially lowered quality factor due to peak spreading.

FIGURE 4.8 *Resonant peaks of each resonator @ 100 mTorr*

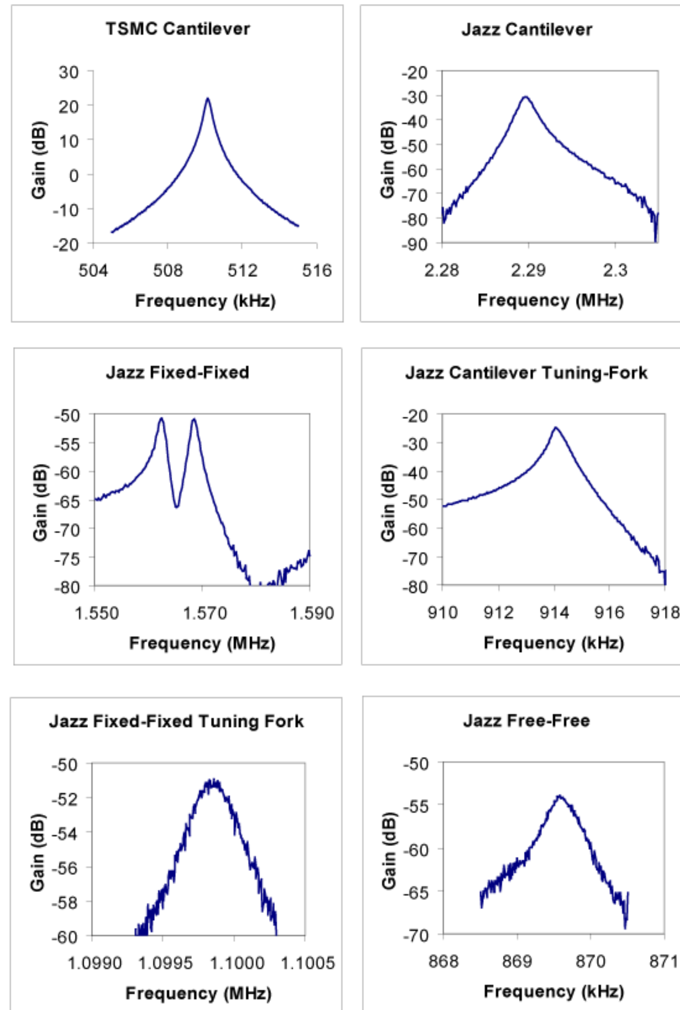

4.4 Data Analysis

4.4.1 Pressure Dependence of Quality Factor

The quality factor dependence on pressure is plotted in Figure 4.9 for the TSMC and Jazz cantilevers, along with the simulated curve based on the analysis in Chapter 2. To give a more helpful representation of the theoretical squeeze-film quality factor, it is calculated assuming the other damping mechanisms are constant with respect to

pressure and at the same level as the measured data. This leads to two simulated curves: one for the TSMC cantilever and one for the Jazz cantilever.

FIGURE 4.9 *Quality factor of the TSMC and Jazz cantilevers as a function of air pressure*

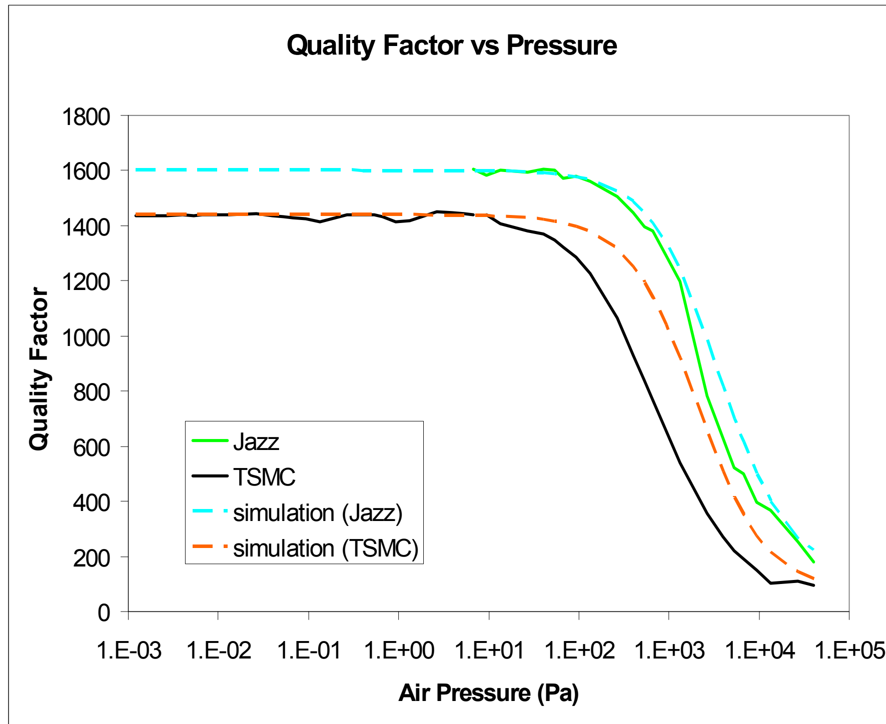

Both measured curves have the same shape as the simulated curves, though the TSMC has more of an offset in pressure than the Jazz curve.

4.4.2 Anchor Design Dependence of Quality Factor

As discussed in Section 2.2, a perfect tuning fork design reduces the energy loss due to anchor dissipation to zero. The energy loss seen, then, is due to the imperfection of the fabricated device in the form of mask misalignment, mask bloat, and lithography imprecision. In addition, a slight mass imbalance is caused by a designed notch in the cross-beam of both the cantilever and fixed-fixed tuning forks near the anchor beam attachment, which is a high-stress point (Figure 3.6). The notch exists to electrically isolate the top metal in each beam. The quarter-wavelength anchor beams should futher reduce the energy loss. The tests of the tuning fork topology showed an decrease in damping due to anchor loss. The frequency of the cantilever tuning fork was 914 kHz, which is lower than the single cantilever, at 2.4 MHz. Since they have different resonant frequencies, the energy loss of the two must be compared with the damping coefficient, b, rather than the quality factor. Extracting b from (2.6) and (2.4) shows that b is 3.84×10^9 for the single cantilever and 1.27×10^9 for the tuning fork cantilever.

The fixed-fixed tuning fork demonstrated a decrease in damping over the single fixed-fixed beam. The frequency of the fixed-fixed beam is decreased by compressive stress, from the expected 6.19 MHz to 1.57 MHz, and the fixed-fixed tuning fork is decreased from 6.19 MHz to 1.10 MHz. Residual stress lowers the effective stiffness of the beam and therefore lowers the resonant frequency [20]. The single fixed-fixed

beam is on the stress-relief platform discussed in Chapter 3, but the tuning-fork is not. The stress-relief platform relieves some of the stress, but not all of it. A calculation indicates that the average residual stress in the 3-metal stack of the beam is 308 MPa. Despite the difference in resonant frequency, the measurements show a marked increase in the quality factor, and this is attributable to the reduction of anchor loss. The damping coefficient, *b*, for the single fixed-fixed beam is 4.41×10^9 and *b* is 1.18×10^9 for the fixed-fixed tuning fork.

The free-free resonator reduces anchor loss by tethering the vibrating beam at the node points, which do not translate. These points do rotate, so some energy will be lost even in a perfect resonator. The free-free beam showed only a moderate increase in quality factor over the Jazz cantilever, and a resonant frequency that is much lower than expected. The anchor loss-reducing design of the free-free beam demands that the tethers be placed at precise points along the beam. Fabrication error such as mask misalignment or mask bloat, which causes a metal layer to increase feature sizes, causes the tethers to shift from the intended node points. Even a slight shift is believed to cause a reduction in quality factor. The designed tethers, due to design rule contraints, are nearly the same width as the beam. This means that the tether attaches to the beam in a relatively large area around the node point, which may cause increased motional coupling to the tether and more damping than intended.

5 Conclusions

The experiments described in Chapter 4 successfully demonstrate that the dominant energy loss mechanism in CMOS-MEMS resonators at atmospheric pressure is air damping, and that the second dominant mechanism is acoustic anchor loss. The theory in Chapter 2 indicates that thermoelastic damping is negligible in the resonators studied here. The other known loss mechanism, internal friction, could be quantified if the acoustic anchor loss is reduced below this mechanism.

The squeeze-film damping theory closely matched the measured data for both the TSMC cantilever and the Jazz cantilever. The Jazz cantilever had an error in the squeeze-film quality factor of about 25%, and the TSMC cantilever had an error of about 69%. One of the assumptions in the theory is that the width and length of the plate are much greater in size than the gap. This work demonstrates that the theory holds reasonably well when relaxing that assumption.

The tests of the tuning fork topology showed an decrease in damping due to anchor loss. The 67% reduction in damping shown in Section 4.4.2 demonstrates that the tuning fork lowers energy loss. To design a more reliable test of the tuning fork, the sin-

gle cantilever to which it is compared should be a crab-leg cantilever anchored at the connection point of the anchor beam on the tuning fork. In essence, the tuning fork should be compared to half of the tuning fork, which would have the same resonant frequency but not the symmetry. This revised test would change only one feature, thus eliminating the effect of changing other aspects of the design. In addition, the notch in the top metal layer near the center of beam connecting the two resonators creates a mass imbalance in the area of maximum stress on the connecting beam and may cause additional internal friction or acoustic damping. This error should be eliminated by switching the nodes that are created by metal 2 and metal 3 on the beam. To test the effectiveness of the quarter-wavelength anchor beams, the tuning fork design should be repeated with varying lengths of the anchor beam, including the calculated quarter- and half-wavelengths.

The fixed-fixed tuning fork provided a 73% decrease in damping over the single fixed-fixed beam. Since this reduction was seen, it demonstrates that anchor loss is more dominant than internal friction. A more decisive test could be gained by redesigning the tuning fork resonators to have the same resonant frequency as their single-resonator counterparts.

The free-free beam showed only a moderate increase in quality factor over the Jazz cantilever, as discussed in Section 4.4.2. To decrease the energy loss of the design, it should be made wider and longer so that the tether beams have a smaller attachment

area relative to the size of the beam. This can be done so that the resonant frequency of the beam remains the same. This design will also reduce the effect of mask misalignment, mask bloat, and lithography errors.

Switching from a DIP in a breadboard to a PCB lowered the direct feedthrough by as much as 50 dB. This, together with the fact that the free-free beam had approximately the same level of feedthrough as the other devices, leads to the conclusion that direct feedthrough is dominated by other capacitances on the chip, and that the square heads separating the drive and sense capacitors in the resonators are not necessary. This conclusion leads to greater design flexibility and the ability to design electrodes along the entire length of some resonators, increasing capacitive sensitivity. Some designs, such as the Jazz fixed-fixed beam, have much higher feedthrough due to routed signals that cross. Future designs should shield all signal lines as well as possible and avoid crossing sensitive lines.

Appendix A: Calculation of Resonant Frequency

A.1 Static Method

The static method of calculating resonant frequency involves lumped modeling involving spring constant, k, and effective mass, m_{eff}. It is an approximation, but is usually faster to compute.

$$\omega_r = 2\pi f_r = \sqrt{\frac{k}{m_{eff}}}. \qquad (A.1)$$

For a point load, the spring constant is calculated by finding the deflection at the point of force application, and dividing the force by it. The deflection is found by the mode shape of the beam. The general solution of static mode shape is [42]

$$y(x) = Ax^3 + Bx^2 + Cx + D. \qquad (A.2)$$

Boundary conditions are then applied to find the specific solution. For a free end, two natural boundary conditions apply:

$$M = EI\frac{d^2y}{dx^2} = 0 \qquad (A.3)$$

and

$$V = EI\frac{d^3y}{dx^2} = F, \qquad (A.4)$$

where M is moment, V is shear force, and F is a concentrated load at that end. If the concentrated load is at a different point, that is where the boundary condition would

occur, and at the free end, V would be zero. At a fixed end, two applied boundary conditions occur

$$y = 0 \tag{A.5}$$

and

$$\frac{dy}{dx} = 0 . \tag{A.6}$$

For a cantilever [42]:

$$y = \frac{F}{6EI}[3(L-a)^2 x - 2L^3 + 3L^2 a - a^3 - \langle x-a \rangle^3] . \tag{A.7}$$

For a fixed-fixed beam:

$$y = \frac{F}{6EI}\left[\frac{(L-a)^2(L+2a)x^3}{L^3} - \frac{(L-a)^2 a x^2}{3L^2} - \langle x-a \rangle^3\right] . \tag{A.8}$$

F is the applied concentrated load, E is Young's modulus, x, a, and L are given in Figure A.1, I is the moment of inertia,

$$I = \frac{hw^3}{12} , \tag{A.9}$$

h is thickness and w is width. $<x-a>^3$ is equal to 0 if $x < a$, and $(x-a)^3$ if $x > a$.

By substituting a for x in the beam shape equation, the deflection at the point of force application is found. The stiffness is then the force, F, divided by the deflection. The F will cancel out. For a cantilever with force at x=0,

$$k = \frac{3EI}{L^3} . \tag{A.10}$$

For a fixed-fixed beam with force at $x=L/2$,

$$k = \frac{192EI}{L^3}. \tag{A.11}$$

Effective mass is a concept that allows the use of lumped modeling. It is derived from conservation of energy. Since maximum potential energy is equal to maximum kinetic energy in a vibrating system,

$$\frac{1}{2}ky_F^2 = \int_0^L \frac{1}{2}m_L v(x)^2 dx = \int_0^L \frac{1}{2}m_L \omega^2 y(x)^2 dx, \tag{A.12}$$

where y_F is the maximum deflection at the point of force application, m_L is the mass per unit length, and ω is the angular velocity of vibration. Solving for ω,

$$\omega^2 = \frac{ky_F^2}{\int_0^L m_L y(x)^2 dx}, \tag{A.13}$$

and combining (A.13) with (A.1) the effective mass is

$$m_{eff} = \frac{m_L \int_0^L y(x)^2 dx}{y_F^2}. \tag{A.14}$$

The effective mass is equal to the actual mass multiplied by a factor, α, that is different for every beam.

$$\alpha = \frac{\frac{1}{L}\int_0^L y(x)^2 dx}{y_F^2} \tag{A.15}$$

Combining (A.10) and (A.11) with (A.14) in (A.1) produces

$$f_r = \frac{1}{8\pi}\sqrt{\frac{1}{\alpha_c}}\sqrt{\frac{E}{\rho}}\frac{w}{L^2} \qquad \text{(A.16)}$$

for the cantilever, where α_c is the effective mass factor for a cantilever, given in (A.15), and

$$f_r = \frac{4}{2\pi}\sqrt{\frac{1}{\alpha_f}}\sqrt{\frac{E}{\rho}}\frac{w}{L^2} \qquad \text{(A.17)}$$

for the fixed-fixed beam, where α_f is the effective mass factor for the fixed-fixed beam.

A free-free beam does not have a static bending shape, as there are no anchors to constrain it. Dynamic analysis must be used to calculate the resonant frequency of a free-free beam.

FIGURE A.1 *Diagrams of a.) cantilever and b.) fixed-fixed beams*

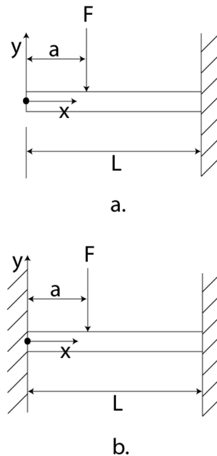

A.2 Dynamic Method

The general eigenfunction for a uniform beam in bending vibration is [43]

$$EI\frac{\partial^4 Y(x)}{\partial x^4} = \omega^2 m Y(x)\,. \tag{A.18}$$

The difference between the initial differential equation for finding the beam shape function in the static case and the dynamic case is the inertial term, the right-hand side of (A.18). The general solution is

$$Y(x) = C_1 \sin\beta x + C_2 \cos\beta x + C_3 \sinh\beta x + C_4 \cosh\beta x\,, \tag{A.19}$$

where β is

$$\beta^4 = \frac{\omega^2 m_L}{EI} \tag{A.20}$$

and m_L is the mass per unit length, and the same boundary conditions are applied as in the static solution. This time, the boundary conditions are used to find the values of β that are valid, which lead to the values of ω that correspond to the resonant frequencies of each mode of vibration. For a cantilever, the boundary conditions lead to

$$\cos\beta L \cosh\beta L = -1\,, \tag{A.21}$$

which, when solved numerically, yields the values of βL: 1.875 for the fundamental mode, 4.694 for the second mode, 7.855 for the third mode, and so on. Substituting these values in to (A.20) allows the solution of the fundamental resonant frequency:

$$f_r = \frac{(1.875)^2}{2\pi}\sqrt{\frac{1}{12}}\sqrt{\frac{E}{\rho}}\frac{w}{L^2} \tag{A.22}$$

For a fixed-fixed beam, the boundary conditions lead to

$$\cos\beta L \cosh\beta L = 1\,, \tag{A.23}$$

which yield βL values of 4.730 for the fundamental mode, 7.853 for the second mode, 10.996 for the third mode, and so on. For a free-free beam, the boundary conditions yield the same βL values as for the fixed-fixed beam. The fundamental frequency is

$$f_r = \frac{(4.73)^2}{2\pi}\sqrt{\frac{1}{12}}\sqrt{\frac{E}{\rho}}\frac{w}{L^2}\,. \tag{A.24}$$

References

[1] Stillman, J., *CMOS-MEMS Resonant Mixer-Filters*, MS Thesis, ECE, Carnegie Mellon University, July 2003

[2] Wong, A.-C., and Nguyen, C.T.-C., "Micromechanical mixer-filters ('mixlers')," *J. Microelectromechanical Systems*, Vol. 13, No. 1, pp. 100-112, February 2004

[3] Bannon, F.D., Clark, J.R., and Nguyen, C.T.-C., "High-Q HF microelectromechanical filters," *IEEE J. of Solid-State Circuits*, Vol. 35, No. 4, pp. 512-526, April 2000

[4] Galayko, D., Kaiser, A., Buchaillot, L., Collard, D., and Combi, C., "Electrostatic coupling-springs for micro-mechanical filtering applications," *Proc. 2003 Intl. Symposium on Circuits and Systems, 25-28 May 2003*, Vol. 3, pp. 530-533

[5] Xie, H., Erdmann, L., Zhu, X., Gabriel, K.J., and Fedder, G.K., "Post-CMOS processing for high-aspect-ratio integrated silicon microstructures," *J. of Microelectromechanical Systems*, Vol. 11, No. 2, pp. 93-101, April 2002

[6] Pourkamali, S., Hashimura, A., Abdolvand, R., Ho, G.K., Erbil, A., and Ayazi, F., "High-Q single crystal HARPSS capacitive beam resonators with self-aligned sub-100-nm transduction gaps," *J. Microelectromechanical Systems*, Vol. 12, No. 4, pp. 487-496, August 2003

[7] Adler, R., "Compact electromechanical filters," *Electronics*, 20, pp. 100-105, April 1947

[8] Johnson, R.A., *Mechanical Filters in Electronics*, New York, Wiley, 1983

[9] Nathanson, H.C., Newell, W.E., Wickstrom, R.A., and Davis, J.R., "The resonant gate transistor," *IEEE Trans. on Electron Devices*, ED-14, pp. 117-133, March 1967

[10] Howe, R.T., "Resonant microsensors," *Tech. Digest, 4th Intl. Conf. Solid-State Sensors and Actuators (Transducers '87), Tokyo, Japan, June 2-5, 1987*, pp. 843-848

[11] Schmidt, M.A., and Howe, R.T., "Resonant structures for integrated sensors," *Tech. Digest, IEEE Solid-State Sensor Workshop, Hilton Head Island, S.C., U.S.A., June 2-5, 1986*, pp. 94-97

[12] Tang, W.C., Nguyen, C.T.-C., and Howe, R.T., "Laterally driven polysilicon resonant microstructures," *Sensors and Actuators*, 20, pp. 25-32, 1989

[13] Tang, W.C., Nguyen, C.T.-C., Judy, M.W., and Howe, R.T., “Electrostatic comb-drive of lateral polysilicon resonators,” *Sensors and Actuators*, A21-A23, pp. 328-331, 1990

[14] Lin, L., Nguyen, C.T.-C., Howe, R.T., and Pisano, A.P., “Micro electromechanical filters for signal processing,” *Micro Electro Mechanical Systems ’92, Travemünde, Germany, February 4-7, 1992*, pp. 226-231

[15] Blom, F.R., Bouwstra, S., Elwenspoek, M., and Fluitman, J.H.J., “Dependence of the quality factor of micromachined silicon beam resonators on pressure and geometry,” *J. Vac. Sci. Tech.*, B10(1), pp. 19-26, January/February 1992

[16] Hosaka, H., Itao, K., and Kuroda, S., “Damping characteristics of beam-shaped micro-oscillators,” *Sensors and Actuators*, A49, pp. 87-95, 1995

[17] Li, B., Wu, H., Zhu, C., and Liu, J., “The theoretical analysis on damping characteristics of resonant microbeam in vacuum,” *Sensors and Actuators*, 77, pp. 191-194, 1999

[18] Chen, H., Drilhole, D., and Robert, O., “Air damping of mechanical microbeam resonators with optical excitation and optical detection,” *Tech. Digest, IEEE/LEOS International Conference on Optical MEMS, August 20-23, 2002*, pp. 61-61

[19] Corman, T., Enoksson, P., and Stemme, G., “Gas damping of electrostatically excited resonators,” *Sensors and Actuators*, A61, pp. 249-255, 1997

[20] Senturia, S.D., *Microsystem Design*, Kluwer, Norwell, Massachusetts, 2001

[21] Veijola, T., Kuisma, H., Lahdenpera, J., and Ryhanen, T., “Equivalent-circuit model of the squeezed gas film in a silicon accelerometer,” *Sensors and Actuators*, A48, pp. 239-248, 1995

[22] Vemuri, S., Fedder, G.K., and Mukherjee, T., “Low-order squeeze film model for simulation of MEMS devices,” *Proc. 2000 Intl. Conf. on Modeling and Simulation of Microsystems Semiconductors, Sensors and Actuators, March 27-29, 2000*, pp. 205-208

[23] Wang, K., Yu, Y., Wong, A.-C., and Nguyen, C.T.-C., “VHF free-free beam high-Q micromechanical resonators,” *Twelfth IEEE International Conference on Micro Electro Mechanical Systems, January 17-21, 1999*, pp. 453-458

[24] Hsu, W.-T., Clark, J.R., and Nguyen, C.T.-C., "Q-optimized lateral free-free beam micromechanical resonators," *11th International Conference on Solid-State Sensors and Actuators, Munich, Germany, June 10-14, 2001*, pp. 1110-1113

[25] Park, Y.H., and Park, K.C., "Coupled substrate-resonator-electrostatic simulation and validation of high-Q MEMS resonator performance," *Tech. Digest, Nanotech 2003*, Vol.1, pp. 412-415

[26] Konno, M., and Nakamura, H., "Equivalent electrical network for the transversely vibrating uniform bar," *J. Acoust. Soc. Amer.*, Vol. 38, pp. 614-622, 1965

[27] Roszhart, T.V., "The effect of thermoelastic internal friction on the Q of micromachined silicon resonators," *Tech. Digest, 4th IEEE Solid-State Sensor and Actuator Workshop, June 1990*, pp. 13-16

[28] Lifshitz, R., and Roukes, M.L., "Thermoelastic damping in micro- and nanomechanical systems," *Physical Review B*, Vol. 61, No. 8, pp. 5600-5609, February 15, 2000

[29] Duwel, A., Weinstein, M., Gorman, J., Borenstein, J., and Ward, P., "Quality factors of MEMS gyros and the rose of thermoelastic damping," *15th IEEE International Conference on Micro Electro Mechanical Systems, January 20-24*, 2002, pp. 214-219

[30] Srikar, V.T., and Senturia, S.D., "Thermoelastic damping in fine-grained polysilicon flexural beam resonators," *J. of Microelectromechanical Systems*, Vol. 11, No. 5, pp. 499-504, October 2002

[31] Matweb, http://www.matweb.com

[32] Stemme, G., "Resonant silicon sensors," *J. Micromech. Microeng.*, 1, pp. 113-125, 1991

[33] Mihailovich, R.E., and MacDonald, N.C., "Dissipation measurements of vacuum-operated single-crystal silicon microresonators," *Sensors and Actuators*, A50, pp. 199-207, 1995

[34] Yasamura, K.Y., Stowe, T.D., Chow, E.M., Pfafman, T., Kenny, T.W., Stipe, B.C., and Rugar, D., "Quality factors in micron- and submicron-thick cantilevers," *J. Microelectromechanical Systems*, Vol. 9, No. 1, pp. 117-125, March 2000

[35] Mohanty, P., Harrington, D.A., Ekinci, K.L., Yang, Y.T., Murphy, M.J., and Roukes, M.L., "Intrinsic dissipation in high-frequency micromechanical resonators," *Physical Review B*, 66, 085416, 2002

[36] Candler, R.N., Li, H., Lutz, M., Park, W.-T., Partridge, A., Yama, G., and Kenny, T.W., "Investigation of energy loss mechanisms in micromechanical resonators," *12th International Conference on Solid State Sensors, Actuators, and Microsystems, Boston, June 8-12, 2003*, pp. 332-335

[37] MOSIS website, http://www.mosis.com/products/fab/vendors/tsmc/

[38] Jazz Semiconductor website, http://www.jazzsemi.com/process_technologies/sige.shtml

[39] Fedder, G.K., *Simulation of Microelectromechanical Systems*, Ph.D. Thesis, UC Berkeley, 1994

[40] Galayko, D., Kaiser, A., Legrand, B., Collard, D., Buchaillot, L., and Combi, C., "High-frequency high-Q micro-mechanical resonators in thick epipoly technology with post-process gap adjustment," *15th IEEE International Conference on Micro Electro Mechanical Systems, January 20-24*, 2002, pp. 665-668

[41] Luo, H., Fedder, G.K., and Mukherjee, T., "Integrated multiple device IMU systems with continuous-time sensing circuitry," *Proc. IEEE Intl. Solid-State Circuits Conf., February 9-13, 2003*, paper 11.7

[42] Young, W.C., *Roark's Formulas for Stress and Strain*, Sixth Edition, McGraw-Hill, New York, 1989

[43] Meirovitch, L., *Analytical Methods in Vibrations*, Macmillan, New York, 1967